An introduction to NMR-based approaches for measuring protein dynamics

Ian R Kleckner[a] and **Mark P Foster**[b,‡]

[a]The Ohio State University Biophysics Program, 484 West 12th Ave Room 776, Columbus, OH, 43210, USA. Kleckner.5@osu.edu

[b]The Ohio State University Biochemistry Department, 484 West 12th Ave Room 776, Columbus, OH, 43210, USA. Phone: (614) 292-1377; Fax: (614) 292-6773; Foster.281@osu.edu

Abstract

Proteins are inherently flexible at ambient temperature. At equilibrium, they are characterized by a set of conformations that undergo continuous exchange within a hierarchy of spatial and temporal scales ranging from nanometers to micrometers and femtoseconds to hours. Dynamic properties of proteins are essential for describing the structural bases of their biological functions including catalysis, binding, regulation and cellular structure. Nuclear magnetic resonance (NMR) spectroscopy represents a powerful technique for measuring these essential features of proteins. Here we provide an introduction to NMR-based approaches for studying protein dynamics, highlighting eight distinct methods with recent examples, contextualized within a common experimental and analytical framework. The selected methods are (1) Real-time NMR, (2) Exchange spectroscopy, (3) Lineshape analysis, (4) CPMG relaxation dispersion, (5) Rotating frame relaxation dispersion, (6) Nuclear spin relaxation, (7) Residual dipolar coupling, (8) Paramagnetic relaxation enhancement.

Keywords

protein dynamics; protein flexibility; NMR

1. Introduction

Although the functions of many proteins can be understood from their time-averaged structure, proteins are inherently flexible at ambient temperature, and this flexibility generally reflects important mechanistic aspects of their function [1,2]. That is, proteins don't simply occupy one structure, rather they are more accurately described by an equilibrating set of time-dependent structures. These distinct conformations are continuously sampled within a hierarchy of spatial and temporal scales ranging from nanometers to micrometers and femtoseconds to hours. Understanding the structural bases of such dynamic processes is important for realizing the full spectrum of macromolecular function and for predicting and engineering protein behavior.

‡Corresponding author: 484 West 12th Ave Room 776, Columbus, OH, 43210, USA. Phone: (614) 292-1377; Fax: (614) 292-6773; Foster.281@osu.edu.

In the context of this review, "protein dynamics" refer to time-dependent fluctuations in structure. These involve mostly internal motions that reflect sampling of distinct conformations on defined timescales (figure 1). It is insufficient to simply describe a protein as "being dynamic", like it is insufficient to simply describe a protein as "having structure". All proteins exhibit dynamics, but important distinctions are found in the timescale in which structural changes occur and in the nature of the corresponding change in atomic coordinates. Indeed, complete structural characterization of a protein requires defining: (i) the three-dimensional position of each atom for each state in the conformational landscape, (ii) the populations of each state ("static flexibility" [3]) via relative energies and (iii) and rates and pathways of inter-state conversion ("dynamic flexibility").

Protein dynamics affect a wide range of functions, such as catalytic turnover of enzymes [2,4,5], signaling/regulation [6] and thermostability [3]. Dynamics affect the rate and pathway of protein folding [7,8] as well as misfolding and aggregation, which can catalyze an array of fatal neurodegenerative diseases [9]. Dynamics can affect binding [10-12] via induced fit or conformational selection [13], allostery [14-20] and the effectiveness of small molecule inhibitors [21-23]. Dynamics can enable some proteins to perform multiple distinct functions [24] and are important for the evolution of novel functions [25,26].

Investigation of this dynamics-function linkage relies upon nuclear magnetic resonance (NMR) due to its exquisite sensitivity to local structure and dynamics in many distinct time windows, each of which may have different functional implications (section 2). By harnessing these unique assets, NMR studies have provided mechanistic detail at unmatched structural resolution into protein folding [7], catalytic turnover of enzymes [2], lowly populated "invisible" excited state structures [27,28] and important thermodynamic quantities including entropy [29-31] and heat capacity [32]. The thermodynamic relationships are extremely insightful because the driving force for any physical process in a biological system is the change in Gibbs free energy (G) which is determined by changes in enthalpy (H), entropy (S) and temperature (T) via $\Delta G = \Delta H - T\Delta S$. Therefore, this relationship fundamentally links structure (H), dynamics (S) and function (G).

Unfortunately, the information derived from NMR does not always explicitly include structural coordinates, thereby limiting certain insights into the structure-dynamics-function linkage. To address this limitation, NMR studies are often complemented with computational simulations of protein dynamics. Conventional molecular dynamics (MD) is the most common approach whereby the three-dimensional positions of each atom in the protein and solvent are computed over time using empirically determined interaction forces [33]. This high-resolution approach is limited to tens of nanoseconds for moderately sized proteins (100-300 residues), but these limits can be extended by applying various simplifications. For instance, course-grained simulations such as principle component analysis (PCA) and elastic network models (ENMs) predict collective motions for relatively large proteins at longer timescales, but are typically only sensitive to backbone topology and not side chain identity [34,35]. These computational approaches are important because they enhance understanding of the motions experimentally observed using NMR [36-40].

Among many experimental methods that can be used to observe and/or infer protein dynamics [1,41], NMR spectroscopy has emerged as a principal tool due to its exquisite resolution, non-perturbing nature, wide range of applications [2,28,42] and solid theoretical foundations [43-47]. This work provides an overview of eight distinct NMR-based methods for studying protein dynamics, with the goal of creating familiarity with the information accessible via NMR and a flavor for its interpretation.

2. NMR introduction

2.1. NMR principles and the three observables (δ, I, λ)

Nuclear magnetic resonance exploits the magnetic properties of certain nuclei [43,47,48]. The phenomenon was first reported in 1946 [49-51] using simple compounds but is now routinely used to study large and complex biomolecules. For proteins, the NMR-active nuclei of interest are the spin ½ isotopes ^{1}H, ^{13}C, ^{15}N and ^{31}P, which exhibit magnetic dipole moments, and the spin 1 isotope ^{2}H, which exhibits both magnetic dipole and quadrupole moments. These isotopes can be introduced in a non-perturbing manner at desired locations within the protein, thus providing many site-specific probes of local structure and dynamics [52,53]. In solution NMR, typically 0.3-0.6 mL of 0.1-5.0 mM sample is loaded into an NMR tube and placed in a strong magnetic field denoted B_0. The bulk magnetic moment for each set of NMR-active isotopes will preferentially align with B_0 along the z-axis of the magnetic field. A weaker magnetic field temporarily applied perpendicular to B_0 rotates this bulk magnetic moment into the transverse (x,y) plane. The bulk moment will then undergo Larmor precession about B_0 akin to a spinning top's angular momentum precessing about the gravity field vector. The nuclei in the sample precess at characteristic rates that differ from one another due to small perturbations in their respective local magnetic fields. These perturbations are influenced by the local structure of both protein and solvent via placement of charged side chains and solutes, aromatic ring currents, bond torsion angles and hydrogen bonding.

The fundamental observable in modern Fourier transform (FT) NMR is the free induction decay (FID). This is a time-dependent current which is induced and detected in the receiver coil of the instrument and results from all the precessing nuclei in the sample. Therefore, the observed FID is the sum of all the individual FIDs for each nucleus, each of which oscillates at a characteristic frequency. The FID loses coherence over time as evidenced by its exponential decay of intensity. The rate of intensity decay is an important NMR observable which can be quantified by the transverse relaxation rate constant R_2 (the inverse of the time constant T_2) via $I(t) = exp(-R_2t) = exp(-t/T_2)$ where $I(t)$ is the FID intensity at time t. Once acquired, the observed FID is Fourier transformed from the time domain to the frequency domain so that three primary observables (chemical shift, δ, intensity, I and linewidth, λ) can easily be studied for each NMR signal (figure 2).

(1) *Frequency* (or *chemical shift*, δ) is the position of the signal in the frequency spectrum and reports on the local chemical environment of the nucleus (determined by electron density and currents). It can be expressed in absolute units as *v (Hz = /sec) or ω (rad/sec) = 2π v(Hz)*, both of which scale with B_0 field strength, or it can be normalized to the field

strength and expressed as parts per million, $\mathrm{ppm}: \delta\,(ppm) = \bar{\omega}\,(ppm) = \dfrac{v\,(Hz)}{\gamma B_0\,(MHz)}$ where γ is the gyromagnetic ratio for the nucleus. Chemical shift is typically interpreted as a metric for local structure and can be used to identify torsion angles, hydrogen bonding, secondary structure elements and the presence of local electric charges and currents [54]. However, much like fluorescence quantum yield or molar ellipticity, this metric is fundamentally limited because the many structural contributions to the chemical shift are difficult to deconvolute. Investigation of the structure-chemical shift relationship is an active and important area of research in NMR [55-57] but is outside the scope of this review. (2) Intensity (*I*) can be quantified by the height of the peak or the volume under the peak in the frequency spectrum. This observable reports on the number of nuclei resonating at a given frequency since each signal is effectively a superposition of the individual nuclei which experience that particular chemical environment. This dimensionless quantity is generally considered relative to other signals in identically-acquired spectra. (3) Linewidth (*λ*) is the

full peak width at half maximum height and reports on the dynamic properties of the molecule in solution, including ~ns molecular rotation and ps-ms internal motion. λ is directly related to the transverse relaxation rate, $R_2\ (Hz) = 1\ /\ T_2\ (sec) = \lambda\ /\ 2\ (Hz)$, and hence λ, R_2 and T_2 are implemented interchangeably to interpret NMR spectra. Importantly, all three observables can be affected by dynamics over the full range of timescales, with the most direct effects arising via the phenomenon of chemical exchange (section 2.2).

2.2. Chemical exchange can directly alter the three NMR observables

Chemical exchange refers to a dynamic process that exposes an NMR probe to at least two distinct chemical environments, or states, in a time-dependent manner. The simplest model of a dynamic process is interconversion between only two states (figure 3, a). This can correspond to a variety of dynamic processes, including exchange between ligand-free ↔ ligand-bound states of a protein, monomer ↔ dimer, protonated ↔ deprotonated, or conformations A ↔ B. Due to its simplicity, the two-state model is the first and foremost employed to interpret experimental data and will often suffice for rigorous analyses as well. Hence, although it is possible to simulate NMR spectra in the presence of more complex dynamics using the McConnell equations [58, 59], this discussion is limited to exchange between just two states. For NMR, the two states have resonance frequencies v_A and v_B and chemical shift difference $\Delta v = /v_A - v_B/$. Importantly, the appearance of the NMR spectrum depends on the populations of each of the states, P_A and P_B, and the relative values of the exchange rate $k_{ex} = k_A + k_B$ and the chemical shift difference Δv. Note that k_{ex} quantifies the average number of stochastic exchange events per unit time and is therefore expressed in / sec ("per second") instead of Hz to avoid the misinterpretation that these events are equally spaced in time like a wave oscillating at some fixed frequency. With that in mind, k_{ex} and Δv can be compared directly since they have the same units; the effect of varying k_{ex} on the NMR spectrum is shown in figure 3, b.

NMR spectra affected by chemical exchange are segregated into three distinct exchange regimes denoted slow ($k_{ex} << |\Delta v|$), intermediate ($k_{ex} \approx |\Delta v|$) and fast ($k_{ex} >> |\Delta v|$). This distinction is made by *comparison* of k_{ex} and $|\Delta v|$ (both in /sec) but not either alone. Furthermore, Δv scales linearly with the B_0 field strength such that increasing B_0 will *decrease* the relative timescale of exchange (i.e., an unchanged k_{ex} compared to an increased $|\Delta v|$).

In the slow exchange regime ($k_{ex} << |\Delta v|$) signals from both states are observed reflecting their distinct chemical shifts, intensities and linewidths. This is because there is not significant A ↔ B interconversion during the frequency detection period of the NMR experiment. In this limit, the intensity of each peak directly reports on the population of that species (provided sufficient inter-scan recovery time, section 2.3). For either state, if the departure rate k is greater than ~10 /sec the signal linewidth will increase due to the depopulation of the state during the ~100 ms detection period. This process directly contributes to the exponential decay of the FID intensity and can be quantified by an increase in transverse relaxation rate via $R_2^{Obs} = R_2^0 + k$ where R_2^0 is the relaxation rate in the absence of exchange.

At the opposite limit of fast exchange, *one* signal is observed with a population-weighted chemical shift $\delta^{Obs} = P_A\delta_A + P_B\delta_B$ and relaxation rate $R_2^{Obs} = P_A R_{2A} + P_B R_{2B}$. This is because there is rapid A ↔ B interconversion and hence averaging during the detection period of the NMR experiment. In intermediate exchange, or coalescence, one signal is observed at a chemical shift between δ_A and δ_B. Importantly, the linewidth of this peak is "exchange broadened" due to interference from A ↔ B interconversion during the detection period. This additional broadening is denoted R_{ex} such that $R_2^{Obs} = R_2^0 + R_{ex}$ where R_2^0 is the relaxation rate in the absence of exchange. This phenomenon is fundamentally different

from the $R_2{}^{Obs} = R_2{}^0 + k$ effect from slow exchange because k enhances relaxation strictly through population-loss without the effect of interference during the acquisition period. Anomalous peak broadening (i.e., $R_{ex} > 0$) is a hallmark of dynamics in the intermediate exchange regime and is utilized extensively in relaxation dispersion (section 3.4). These three exchange regimes reflect simplifying limiting cases of chemical exchange. However, dynamic processes may be observed anywhere along this continuum.

2.3. Four basic steps to any NMR experiment

NMR experiments manipulate nuclear magnetization via sequences of radio frequency (RF) pulses applied at specific times for specific durations. Despite the apparent complexity of many NMR experiments, they are often constructed from simpler building blocks that fit within a common architecture of four basic steps: (1) Recovery, (2) Preparation, (3) Evolution and (4) Detection (figure 4). The four steps are typically repeated ~2-32 times to increase the signal to noise ratio via signal averaging.

1. The recovery period (or inter-scan delay) is required to permit restoration of equilibrium magnetization used for detection. After each FID is acquired, the magnetization is "exhausted" and must be restored to equilibrium before preparation of the next FID. The duration of this period typically ranges from 0.5 – 5.0 sec and is directly determined by the longitudinal relaxation rate R_1 of the nuclei of interest with the guideline $T_{recovery} = (3\text{-}5) / R_1$. The long duration of this period is the primary limitation to rapid acquisition of NMR data and hence reducing $T_{recovery}$ is an active area of NMR research (RT-NMR section 3.1).

2. The preparation period is used to select the nucleus and magnetization state of interest. Protein NMR typically utilizes the nuclei ^1H, ^{13}C, ^{15}N or ^{31}P and single-quantum (SQ) magnetization. Other magnetization types such as multiple quantum (MQ), zero quantum (ZQ) and double quantum (DQ) exhibit altered relaxation properties and thus provide independent measures of local structure and dynamics for each nucleus.

3. The evolution period contains delays required to permit evolution of additional time-dependent phenomena, each of which is dedicated an additional "dimension". Often, an additional dimension is used to create a ^1H-X correlation spectrum by evolving the chemical shift of an attached nucleus $X = {}^1H$, ^{13}C, ^{15}N or ^{31}P. In this case, the incremented time delay is necessary to indirectly sample the FID for the attached nucleus. In some dynamics experiments, an additional dimension is used to evolve relaxation and/or chemical exchange. Many of the NMR experiments described here are simply distinguished by their use of the relaxation delay in the evolution period. Since each dimension requires incrementation of an independent delay, the total duration of these multi-dimensional NMR experiments can become prohibitively long (12-72 hours).

4. The detection period directly observes the FID. Its time-dependent intensity is modulated in a manner that encapsulates the effects of the first three steps.

3. NMR methods

Biological functions span a range of timescales depending on the underlying conformational changes of cellular proteins. These changes can be studied using an array of NMR experiments that are like windows into the dynamic landscape of a protein (figure 5). Accurately mapping this landscape often requires a variety of experimental observables that adhere to a self-consistent model with the desired predictive power.

Before approaching these individual methods, it is important to consider the strengths and limitations inherent to *any* NMR-based approach. First and foremost, NMR provides access to site-specific probes of local structure and dynamics with unmatched coverage across almost every atom in the protein [52]. The probes are essentially non-perturbing except for the change in nuclear mass and resulting kinetic isotope effect, therefore alleviating concerns for unintentionally altering the essential properties of structure, dynamics and function. Furthermore, minor changes in these essential properties can be detected via the three NMR observables and hence an NMR spectrum is acknowledged as a comprehensive "molecular fingerprint". Proteins can be studied in solution state under native conditions using a wide range of solvents or in the crystalline or amorphous solid state. Finally, it is expected that NMR will make greater contributions to future scientific investigations due to continued development of theory, instrumentation and application [60].

The most fundamental and practical limitation of NMR is the poor sensitivity of signal detection due to the low characteristic energy of magnetic spin transitions. This makes NMR costly in time and quantity of material and places a relatively low upper-limit on the size of molecules which can be studied (typically <50-100 kDa for structures and up to 1 MDa for specialized studies) [53,61]. NMR is also financially costly due to the technology required to manufacture both high-field instrumentation and isotopically labeled samples.

Spectral crowding is frequently cited as a limitation to NMR but this is simply a result of one of its greatest assets: namely the vast number of structural probes available by default. For comparison, NMR can simultaneously detect tens to hundreds of endogenous probes per molecule whereas fluorescence methods use only one to three. Spectral crowding can be reduced by preparing samples with fewer structural probes per molecule. For example, isotopic labeling can be limited to a subset of amino acid types and/or protein domains [62]. Unfortunately, site-specific labeling methods tend to reduce the yield of labeled protein production and thus create additional unique challenges.

In addition to the specific limitations of NMR, it is important to address the general limitations of all ensemble spectroscopic methods. In order to describe molecular dynamics as exchange between multiple states, it is necessary to obtain a metric by which these states can be distinguished. Fortunately, NMR provides many observables and interpretables which may suit this task, including chemical shift δ, relaxation rates R_1 and R_2, paramagnetic relaxation enhancement Γ, correlation function for internal motion $C(\tau)$, residual dipolar coupling RDC and scalar coupling J. Similarly, fluorescence and absorbance spectroscopy provide unique metrics including wavelength-dependent quantum yield $\Phi(\lambda)$, fluorescence lifetime τ and fluorescence anisotropy. Importantly, if there is no observable difference in a particular metric between the exchanging states then it does not *necessarily* mean there are no dynamics. Instead, it means there is simply no detectable difference in that observable between the multiple states under those experimental conditions.

To expound upon this general limitation, consider the following two cases: (1) A dynamic region of a protein may appear static if the chemical shifts of the exchanging states are equivalent (e.g., a side chain probe waving in the solvent may experience a constant $\delta(solvent)$, despite its flexibility). (2) A static region of a protein may appear dynamic if there is relative motion of an adjacent chemical group (e.g., a rigid backbone probe next to a flexible charged side chain will experience a time-dependent δ despite its rigidity). Furthermore, some dynamic processes may not be visible within a particular experimental window without changing the rate of the process, the populations of the species or the effective exchange regime. Such optimization can often be accomplished by controlling conditions such as temperature, solvent viscosity, ligand concentration, protein sequence, pH or magnetic field strength B_0.

With these general assets and limitations in mind, eight individual NMR-based methods can be properly introduced. The following sections are roughly arranged by increasing experimental complexity and the observable timescale of the dynamic exchange τ_{ex}.

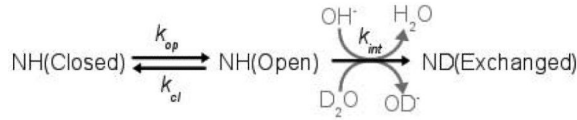## 3.1. Real-time (RT) NMR (τ_{ex} > 1 sec; k_{ex} < 1 /sec)

In this powerful yet simple approach, dynamic processes on the ~sec timescale are directly detected by quantifying the time-dependence of NMR signal intensities [63]. Physical processes on this timescale include protein folding, solvent hydrogen-exchange and relatively slow conformational changes such as *cis-trans* proline isomerization and domain movements that may directly affect catalytic turnover rates. The real-time (RT) NMR experiment is performed by initiating the physical process of interest then rapidly acquiring a sequence of NMR spectra. A special injection apparatus or application of laser light [64] can streamline the initiation process within the NMR tube to study protein folding [65], ligand binding or conformational changes. The sequence of NMR spectra often demonstrate a progressive weakening of an initial set of signals and a progressive strengthening of a new set of signals resulting from time-dependent changes in the populations of different species and/or local structures (i.e., revealing the kinetics of interconversion). An example result is illustrated in figure 6.

The signal intensities from a series of spectra as a function of the time of acquisition are then fitted to an appropriate model such as exponential conversion from A→B (figure 6, b). Provided multiple signals per state, the rate of population change can be quantified in a site-specific manner to determine whether structural changes are concerted or whether different parts of the molecule exchange at different rates. Since each time point requires a single NMR spectrum, RT-NMR had historically been limited to 1D spectroscopy and/or relatively slow kinetic processes *($\tau_{ex} = 1/k_{ex}$ ~ minutes)*. Recent advances in hardware and methodology have enabled 2D RT-NMR by reducing the acquisition time from ~10 min to as low as 0.8 seconds per 2D spectrum [60]. This has been accomplished via an array of strategies involving (1) simultaneous evolution of additional frequency dimensions [66, 67], (2) spatially encoding an additional frequency dimension via pulsed-field gradients [68], (3) reducing inter-scan delay by storing magnetization on fast-relaxing nuclei during recovery [69, 70] and (4) employing additional pulses to enhance longitudinal relaxation [71]. Not surprisingly, combination of these strategies yields a superior cumulative effect [60, 72]. Although RT-NMR is not nearly as sensitive nor rapid as its fluorescence and absorbance counterparts (e.g., stopped-flow dead time is a mere 1-2 ms), recent progress in reducing these limitations indicates an exciting trajectory for current and future applications.

One particularly noteworthy application of fast-acquisition RT-NMR involves the use of the Fluid-Turbulence Adapted (FTA) SOFAST experiment to study folding of the protein α-lactalbumin upon pH jump using a rapid-mixing apparatus [73]. After a post-mixing dead time of 2 sec, each 2D spectrum was acquired in a mere 10 sec, revealing distinct signals from both the molten globule state and the folded state of the protein (figure 7, a). Time-dependent intensities of 92 signals from the folded state and 5 signals from the molten globule state fit well to a single-exponential with τ_{ex} = 109 ± 5 sec, consistent with a global two-state folding pathway (figure 7, b and section A.1). These results are consistent with prior fluorescence studies but yield important additional insights by providing comprehensive structural coverage of the folding event without the need to introduce additional probes via mutations and/or exogenous fluorescence labeling. In this case, there appear to be no local structural effects on the folding rate at this timescale as evidenced by the uniform τ_f values extracted from the fits (figure 7, c).

RT-NMR can also be used to study the dynamic behavior of proteins via hydrogen-deuterium exchange (HDX) by monitoring the exchange of hydrogen atoms between the

protein and the solvent [74,75]. HDX NMR utilizes experiments that yield ^{1}H as visible but ^{2}H as *invisible*. In a typical experiment, a protein bearing [1]H (protons) is exposed to a solvent containing deuterium (D_2O; D = [2]H). As the exchangeable hydrogen atoms on the protein are replaced with those from solvent, ^{1}H is replaced by ^{2}H and hence the observable ^{1}H signals decay in intensity over time. HDX NMR is typically performed by monitoring exchange of backbone amide protons (H^N), and interpreted using the Linderstrom-Lang model [76]:

$$NH(Closed) \underset{k_{cl}}{\overset{k_{op}}{\rightleftharpoons}} NH(Open) \overset{\substack{OH^- \quad H_2O \\ k_{int}}}{\underset{D_2O \quad OD^-}{\longrightarrow}} ND(Exchanged)$$

In this model, each amide NH "breathes" via the closed $\leftrightarrow$ open equilibrium between states that are protected from exchange (*Closed*) to states that are fully exposed to solvent (*Open*). Once open, the H^N atom has an *opportunity* to be exchanged with the solvent. The intrinsic solvent-exchange rate k_{int} depends on local amino acid sequence, temperature and pH in an empirically predictable manner [77]. Importantly, k_{int} is minimized at pH ~2 and increases by a factor of 10 for each unit of pH change from this value (n.b., at pH < 2 hydrogen exchange is acid-catalyzed via [H^+] and [D^+] while for pH > 2 it is base-catalyzed via [OH^-] and [OD^-]). Although this method is typically used for amide hydrogens on the protein backbone and side chain, it generally applies to any exchangeable hydrogen [78,79].

HDX is usually performed under one of two distinct regimes of intrinsic exchange rate denoted EX1 (fast) and EX2 (slow). The EX1 limit corresponds to a regime in which the rate of intrinsic exchange is much faster than the rate of re-protection ($k_{int} >> k_{cl}$). Thus, in this regime the observed exchange rate reflects the *rate* of opening $k_{ex}^{Obs} \approx k_{op}$ (i.e., each opening event results in exchange). For proteins, the EX1 limit is typically sampled at high pH or in the presence of denaturants. The more commonly employed EX2 limit corresponds to slow exchange ($k_{int} << k_{cl}$) and the observed exchange rate reflects the *equilibrium* between the *Open* and *Closed* states: $k_{ex}^{Obs} \approx k_{int}\left(k_{op}/k_{cl}\right)=k_{int}K_{op}$. Therefore, in the EX2 regime, k_{ex}^{Obs} does not reflect the *kinetics* of protein breathing but rather the *thermodynamic* probability of the protein being in the *Open* state. It is not always possible to select the exchange regime through manipulation of experimental conditions, but it can be determined from the pH-dependence of k_{ex}^{Obs}. Regardless of exchange regime, HDX NMR can be performed in two distinct experimental modes denoted "native state" and "pulsed-quench".

In native state HDX, real-time NMR is used to quantify the deuteration-rate k_{ex}^{Obs} via the time-dependent reduction in [1]H^N signal intensity after exposure of the folded protein to D_2O (e.g., figure 6 with no signal for the B state). Native state HDX typically corresponds to the EX2 regime, and thus yields estimates of the equilibrium constant for opening via $K_{op}=k_{op}/k_{cl}=k_{ex}^{Obs}/k_{int}$ and the Gibbs energy of opening $\Delta G_{op} = -RT\ln(K_{op})$, where R is the gas constant and T is the absolute temperature.

In an interesting example of native state EX2-HDX NMR, experiments on the two-domain protein γs-crystallin were performed to understand the mechanism of an aggregation-causing mutation *Opj* involving a Phe9→Ser mutation in the amino-terminal (NT) domain [80]. NMR HDX data showed that upon mutation, the average structure of the protein is preserved but its stability is diminished. Determination of the site-specific K_{op} for both the wild-type protein (WT) and *Opj* (figure 8) showed that destabilization is rooted in only the NT domain of *Opj* as opposed to the entire protein.

Although amides in the EX1 limit often exchange too quickly to be detected via conventional RT-NMR, the FTA-SOFAST 2D NMR method has been successfully applied to study EX1-HDX of human ubiquitin [73]. For rapidly exchanging amides, pulsed-quench HDX can be used to study ~ms protein folding in conjunction with mass-spectrometry or NMR. Since this is not exclusively an NMR-based approach, the interested reader is referred elsewhere [81].

3.2. EXchange SpectroscopY (EXSY) ($\tau_{ex} \approx$ 10-5,000 ms; $k_{ex} \approx$ 0.2-100 /sec; slow exchange $k_{ex} \ll \Delta v$)

EXchange SpectroscopY (EXSY), also known as the zz-exchange experiment, has been in use since at least 1979 [82] to quantify dynamic processes in the 10-5,000 ms time window [45]. Physical processes in this time window include slow conformational changes such as domain movement [83,84], ligand binding [85-87] and release [88], topological interconversion of secondary structure [89,90] and *cis-trans* isomerization [91], all of which may affect catalytic turnover rates in enzymes [2,88,92,93]. EXSY requires that the dynamic process is in the slow exchange regime where each structural probe reveals a unique *set* of signals *($k_{ex} \ll |\Delta v|$,* figure 3). In this case, standard NMR methods may be able to assign each signal to its structural location and hence the extra signals resulting from exchange are clearly identified (e.g., two signals corresponding to the H^N of Ala 12 indicates exchange at this location in the structure). Alternatively, EXSY can be used to assign these signals while simultaneously quantifying the underlying exchange kinetics.

Figure 9 illustrates the use of EXSY for a structural probe exchanging between two states A and B with chemical shifts v_A and v_B, respectively. Because this experiment directly quantifies populations from peak intensities, it is important that the recovery period be long enough to restore Boltzmann equilibrium magnetization if the T_1 relaxation time differs for the two states (i.e., if $T_{1A} \neq T_{1B}$, then $T_{Recover}$ should be at least $3T_1$, figure 4). After recovery and preparation, each structural probe in each molecule is labeled with its chemical shift to identify its current state. During the evolution period, magnetization is stored as longitudinal (along z, the direction of B_0) for an exchange time T during which A↔B interconversion will continue to occur (hence "zz-exchange"). The z-magnetization is subject to T_1 (but not T_2) relaxation and therefore can "survive" exchange times of up to ~5 sec. The upper limit on the exchange time depends entirely on the site-specific T_1 which ranges from 1-8 sec for 10-60 kDa protein at 25°C, and will generally increase with B_0 field strength and decrease with temperature (n.b., EXSY represents a rare case in which a longer T_1 is advantageous). At the end of this delay, some of the spins that were in state A before the delay are now in state B, and vice-versa, provided $k_{ex} \geq 1/T$. The chemical shifts are recorded again in the detection period to identify each structural probe in each molecule with its current state. This experiment yields a 2D spectrum with up to four signals per exchanging structural probe corresponding to two diagonal peaks, *AA* and *BB*, and two crosspeaks indicating exchange $A \xrightarrow{T} B$ and $B \xrightarrow{T} A$ (figure 9, b).

Typically, a series of 2D spectra (i.e., 5-20) are acquired with different values of T (10-5,000 ms) to generate "build-up curves" from the four measured intensities (figure 9, a). These data are fit to an exchange model to extract kinetic rates of interconversion. For two-state exchange, three equations describe the three unique build-up curves using the parameters P_A, P_B $(= 1 - P_A)$, k_{ex} $(= k_A + k_B)$ and R_1 (assuming $R_{1A} = R_{1B}$, though this need not be the case [45]):

$$I_{AA}(T) = P_A(P_A + P_B \exp(-k_{ex}T))\exp(-R_1T)$$
$$I_{BB}(T) = P_B(P_B + P_A \exp(-k_{ex}T))\exp(-R_1T)$$
$$I_{AB}(T) = I_{BA}(T) = P_AP_B(1 - \exp(-k_{ex}T))\exp(-R_1T)$$

EXSY may be limited by spectral crowding and/or poor sensitivity because it functions by introducing additional, often weak, signals into the spectrum. Practically though, many EXSY studies only require a few structural probes to address the questions of interest (as opposed to the tens of structural probes typically required for other NMR-based techniques). For example, in studies of the α_7 annulus of the 20S proteasome core particle, two crucial methionine methyl probes were sufficient to provide unique insight into motions vital to its catalytic mechanism [83] (figure 10). Studying this massive 180 kDa complex was made possible via special methyl group labeling and transverse relaxation optimized spectroscopy (TROSY) [94].

EXSY can also be used to study protein-solvent hydrogen exchange rates that are too fast for RT-NMR (section 3.1). Exchange rates in the range $k_{ex}^{Obs} \approx$ 0.1-50 /sec can be measured by sampling the time-dimension indirectly via the incremented exchange delay. In general, the exchange delay permits $H^N \leftrightarrow H_2O$ exchange, which may place previously-magnetized protons from solvent (^1H_2O) onto the protein. Therefore, each signal in the spectrum results from an H^N atom that has exchanged with H_2O. Build-up curves are constructed from exchange-delay-dependent signal intensities to quantify the site-specific rate of exchange k_{ex}^{Obs}. A variety of solvent EXSY methods are available, each of which circumvents some limitations of their older counterparts: MEXICO [95], a NOESY-based method [96], WEX-II [97], CLEANEX-PM [98], a diffusion-based method [99] and most recently SOLEXSY [100].

For example, a comprehensive study of solvent amide exchange in the protein barstar revealed close coupling between the native-state dynamics measured by NMR and denaturant-induced folding and unfolding rates measured by stopped-flow fluorescence [101]. In this study, the exchange rates of 44 amides were independent of pH and thus in the EX1 regime whereas another 20 switched from EX2 to EX1 by increasing pH in the range 6.5-10. By quantifying site-specific opening and closing rates in the range $k_{op} =$ 0.2-40 /sec and $k_{cl} =$ 10-2,000 /sec, the investigators were able to describe a model in which a minor state observed via NMR corresponds to a distinct unfolding intermediate observed via fluorescence. Overall, EXSY methodology is mature except for incremental improvements in sensitivity and resolution for large molecules via the TROSY effect [86,102].

3.3. Lineshape analysis ($\tau_{ex} \approx$ 10-100 ms; $k_{ex} \approx$ 10-100 /sec; slow-intermediate exchange $k_{ex} \leq \Delta\nu$)

Lineshape analysis is a relatively straightforward approach to interpretation of NMR spectra reporting exchange in the 10-100 ms time window. Physical processes in this time window include binding [85,103-105] and slow-intermediate conformational changes such as small domain movements that could affect catalytic turnover rate and allostery [106]. Lineshape analysis rests upon well-defined theoretical work by McConnell established over half a century ago [59]. Typically, a series of spectra are acquired along a titration coordinate such as ligand concentration (e.g., figure 11), temperature or pH to observe their incremental effect upon the three NMR observables. The spectra in the series may differ as per the principles of chemical exchange, which compare $\Delta\nu$ and $k_{ex} = k_A + k_B$ (figure 3).

In the example shown in figure 11, distinct signals can be observed for the free and bound states of the protein, at ν_P and ν_{PL} respectively. The appearance of the spectra (i.e., the exchange regime: slow, intermediate or fast) is strongly affected by the ligand binding affinity. This is because a tighter-binding complex yields a longer-lived bound state and hence slower exchange between free (P) and bound (PL) states during signal detection. As discussed above, if there is significant interconversion during the ~100 ms detection period, the observed signal(s) will be broadened and/or averaged among the exchanging states (figure 11, b, c).[1]

In practice, lineshape analysis is not limited to the two-state model and therefore it can also be used to study exchange processes involving intermediate states. This is exemplified in a lineshape study of ligand binding by SH2 domain mutants [104]. In this example, spectra from peptide ligand titrations of the wild-type SH2 exhibited signals from the free and bound protein and fit well to a two-state exchange model (figure 12, a). These states appear to exchange in the intermediate-fast regime as indicated by the gradual "marching" of the signal from the P state to the PL state throughout the course of the ligand titration. In contrast to the wild-type domain, titrations conducted with a mutant SH2 domain (P395S) revealed an intermediate state that required a more complex exchange model for fitting the lineshapes (figure 12, b). Interestingly, for the P395S mutant domain, titration spectra revealed remarkable complexity in the ligand binding process. That is, spectra from some of the resonances were too complex to be accurately modeled (see asymmetric line shapes in figure 12, c). This complexity may result from multiple free and/or bound conformations along the titration coordinate. Importantly, the variation in site-specific titration behavior observed throughout the protein reveals that site-specific protein-ligand interactions cannot always be presented on a global level.

Lineshape analysis is primarily limited by degeneracy in chemical shift and large linewidths that lead to signal overlap. As explained in the introduction to section 3, in order to distinguish the exchanging states there must be some quantifiable difference in an observable metric. To address these limitations, isothermal titration calorimetry (ITC) experiments are commonly incorporated to provide an independent measure of the binding thermodynamics. This combined NMR lineshape/ITC approach has been used to study RNase A [103,105] and an SH3 domain [85] among others, using global analysis software [107,108].

3.4. Carr-Purcell Meiboom-Gill Relaxation Dispersion (CPMG RD) ($\tau_{ex} \approx$ 0.3-10 ms; $k_{ex} \approx$ 100-3,000 /sec; intermediate-fast exchange $k_{ex} \approx \Delta\nu$)

Carr-Purcell Meiboom-Gill relaxation dispersion (CPMG RD) is a powerful approach to obtaining kinetic, thermodynamic and structural information for exchange processes in the 0.3-10 ms time window (introductory [5,44], more comprehensive [45,46]). This method was first described in the 1950s [109-111], but was not widely used to study protein

---

[1]The on-rate for protein-ligand binding is typically limited by diffusion (10^6-10^8 /M/sec) and therefore the binding affinity $K_A = 1 / K_d = k_{on} / k_{off}$ is often determined by the off-rate. Provided values of K_d and k_{on}, the exchange rate between free and bound protein states P and PL is given by $k_{ex} = [PL]k_{off} + [P][L]k_{on} = k_{on} ([PL]K_d + [P][L])$ where *[P], [L]* and *[PL]* are concentrations of free protein, free ligand and protein-ligand complex, respectively. These values can be obtained from the standard binding quadratic

$$[PL] = \frac{1}{2}\left(P_{tot} + L_{tot} + K_d - \sqrt{(P_{tot} + L_{tot} + K_d)^2 - 4P_{tot}L_{tot}}\right)$$ derived using mass balance. To exemplify the determinants of the exchange rate k_{ex}, consider the following hypothetical system. An NMR sample contains 1 mM protein (P_{tot}) and 1 mM ligand (L_{tot}), which exhibit an association rate constant $k_{on} = 10^7$ /M/sec. If the K_d is 1 mM (weak binding), $k_{ex} = 7.6$ /sec and the signals may be exchange-broadened. On the other hand, if the K_d is 1 nM (tight binding), k_{ex} is reduced to 2×10^{-5} /sec ≈ 0 (i.e., virtually no exchange). For this same system, if the total ligand concentration is increased to 10 mM, then k_{ex} is increased to 18 /sec if $K_d = 1$ mM but remains nearly zero if $K_d = 1$ nM. These examples illustrate how the ligand concentration may or may not affect the total exchange rate and therefore the observed NMR signal(s).

dynamics until about fifteen years ago, accompanying advances in spectrometer hardware, experimental design [112,113] and isotopic labeling strategies [114]. Dynamic processes in this time window include side chain reorientation, loop motion, secondary structure changes and hinged domain movements [92,105,115,116]. Such motions may affect processes including ligand binding and release [88,103,117-121], folding and unfolding events [7,122-125], allostery [118,119,121] and the rate of catalytic turnover [126-129]. CPMG RD NMR requires an exchange process in the intermediate-fast regime ($k_{ex} \approx \Delta v$) such that the observed signal exhibits an enhanced relaxation rate $R_2^{Obs} = R_2^0 + R_{ex}$ and a broadened linewidth $\lambda = 2R_2^{Obs}$ (figure 3). Although this "chemical exchange broadening" can obscure the observables, it also reflects the underlying protein dynamics and can be exploited for quantitative study. The principle of CPMG RD is to refocus exchange broadening (i.e., reduce or "disperse" R_{ex}) by applying a series spin-echo pulse elements to transverse magnetization during a special relaxation delay (figure 13). The spin-echo element is denoted τ-180-τ where τ is a delay period (~0.25-25 ms) and 180 is a 180° radio-frequency (RF) pulse applied along the ±x or ±y axis.

In general, the spin-echo can refocus a set of magnetization vectors if each individual vector exhibits the same *average* chemical shift during the first and second τ period (i.e., if $<\omega_{\tau 1}>$ = $<\omega_{\tau 2}>$ for each spin). However, if exchange causes a spin to experience a different chemical shift during one τ period and it does not return symmetrically in the other τ period to "compensate", its magnetization will not be refocused at $t = 2\tau$ (n.b., this may occur if $1/k_{ex} \approx \tau$). This results in incomplete refocusing among the ensemble of molecules and therefore leads to signal broadening. The degree of refocusing achieved by the spin-echo element depends on the difference between the average shifts in the first and second τ periods $|<\omega_{\tau 1}> - <\omega_{\tau 2}>|$, with a larger difference resulting in more broadening (n.b., the maximum value of this difference is given by $|v_A - v_B|$). Importantly, as the duration of the τ period is reduced compared to the exchange time $1/k_{ex}$, there will be less signal broadening because the probability of exchange during τ is reduced. The CPMG RD experiment quantitatively explores the relationship between signal broadening and the duration of the spin-echo delay τ.

In practice, a series of NMR spectra (for proteins, usually 2D ^{1}H-^{15}N or ^{1}H-^{13}C) are recorded containing a fixed relaxation time T_{CPMG} (~20-50 ms for large-small molecules), during which a variable number of spin-echos with different values of τ are applied sequentially (i.e., τ-180-τ, τ-180-τ, …) (figure 14). Each value of τ can alternatively be expressed as a CPMG frequency, $v_{CPMG} = 1 / (4\tau)$ that quantifies the rate of precession of magnetization about the axis of the applied RF pulse; typically 10-20 spectra are acquired using $v_{CPMG} \approx$ 50-1200 Hz. Importantly, the effective relaxation rate R_2^{Obs} is altered in a v_{CPMG}-frequency-dependent manner such that significant refocusing is typically achieved when v_{CPMG} exceeds half the exchange rate k_{ex}. The relationship between the *amount* of refocusing via R_2^{Obs} and the CPMG frequency is precisely the information used to fit the model of exchange.

Fitting two-dimensional heteronuclear (^{1}H-X) CPMG RD data is typically accomplished using one of at least three distinct types of equations describing a two-state exchange model (figure 3, a) [44]. (1) The Carver-Richards equations (eq. 1a-e) are valid for any exchange regime [130]. This is the preferred method for analysis because kinetic, thermodynamic and structural information can be extracted independently. (2) The Ishima-Torchia equation (eq. 2) is valid for skewed populations ($P_B < P_A$) [131] and (3) the fast-exchange equation (eq. 3) is valid when $k_{ex} > \Delta v$ [110, 132]. In the following equations, τ is half the delay between 180 degree pulses in the CPMG block (i.e., τ-180-τ, τ-180-τ, τ-180-τ, etc.) and ω (rad/sec) = $2\pi \cdot v$(Hz).

$$R_2^{Obs} = \frac{1}{2}\left(R_{2A}^0 + R_{2B}^0 + k_{ex} - \left(\frac{1}{2\tau}\right)\cosh^{-1}\left(D_+\cosh\left(\eta_+\right) - D_-\cos\left(\eta_-\right)\right)\right) \tag{1a}$$

$$D_\pm = \frac{1}{2}\left(\pm 1 + \frac{\psi + 2\Delta\omega^2}{\left(\psi^2 + \varsigma^2\right)^{1/2}}\right) \tag{1b}$$

$$\eta_\pm = \left(\frac{2\tau}{\sqrt{2}}\right)\left(\pm\psi + \left(\psi^2 + \zeta^2\right)^{1/2}\right)^{1/2} \tag{1c}$$

$$\psi = \left(R_{2A}^0 - R_{2B}^0 - P_A k_{ex} + P_B k_{ex}\right)^2 - \Delta\omega^2 + 4P_A P_B k_{ex}^2 \tag{1d}$$

$$\zeta = 2\Delta\omega\left(R_{2A}^0 - R_{2B}^0 - P_A k_{ex} + P_B k_{ex}\right) \tag{1e}$$

$$R_2^{Obs} = R_2^0 + \frac{P_A P_B \Delta\omega^2 k_{ex}}{k_{ex}^2 + \left(P_A^2\Delta\omega^4 + 144/\left(16\tau^4\right)\right)^{1/2}} = R_2^0 + \frac{\phi_{ex}k_{ex}}{k_{ex}^2 + \left(P_A^2\Delta\omega^4 + 144/\left(16\tau^4\right)\right)^{1/2}} \tag{2}$$

$$R_2^{Obs} = R_2^0 + \left(\frac{P_A P_B \Delta\omega^2}{k_{ex}}\right)\left(1 - \frac{2\tanh\left(k_{ex}\tau\right)}{2k_{ex}\tau}\right) = R_2^0 + \left(\frac{\phi_{ex}}{k_{ex}}\right)\left(1 - \frac{2\tanh\left(k_{ex}\tau\right)}{2k_{ex}\tau}\right) \tag{3}$$

Equations (2) and (3) are clearly simpler than the Carver-Richards analysis and are sometimes unjustifiably used for this reason alone (n.b., Carver-Richards analysis can easily be programmed for fitting via standard computational tools despite its apparent complexity). However, equation (3) is a justified approach in the case of fast exchange wherein the parameters P_A, $P_B = 1-P_A$ and $\Delta\omega$ are convoluted into a single parameter $\Phi_{ex} = P_A P_B \Delta\omega^2$. This situation is generally undesirable because it precludes independent interpretation of populations and chemical shift differences (discussed further in RF RD section 3.5). Therefore, in the absence of fast exchange the Carver-Richards analysis is the method of choice, but for fast exchange equation (3) is a reasonable simplification.

The following identifies the assets and limitations of the Carver-Richards analysis of two-dimensional heteronuclear-correlated ^{1}H-X (X = ^{13}C, ^{15}N) spectra by discussing the 4-6 parameters which can be uniquely determined in the absence of fast exchange. (1, 2: $\Delta\omega_H$, $\Delta\omega_X$) The chemical shift differences between the A and B states for ^{1}H and X, denoted $/\Delta\omega_H/ = /\omega_H^A - \omega_H^B/$ and $/\Delta\omega_x/ = /\omega_x^A - \omega_x^B/$. Note that dispersion experiments are designed detect particular combinations of $\Delta\omega_H$ and $\Delta\omega_X$ and hence may fix $/\Delta\omega_H/ = 0$, or $/\Delta\omega_X/ = 0$ in subsequent analysis [122]. (3, 4: k_A, k_B) The kinetic (and therefore thermodynamic) information is provided equivalently by either k_A and k_B, or k_{ex} and P_A. k_A and k_B are the rates of exchange from A→B and B→A respectively, $k_{ex} = k_A + k_B$ is the total

rate of exchange and P_A is the equilibrium population fraction of state A with

$P_A + P_B = 1.$ $(5,6{:}R_{2A}^0, R_{2B}^0)$ The transverse relaxation rate of each state in the absence of exchange, which are often assumed to be equal, denoted $R_2^0 = R_{2A}^0 \approx R_{2B}^0$ [133]. Note that the NMR signal for the B state is not directly detected because its intensity is too low and/or its linewidth is too large. However, RD can be used to quantify the structure and dynamics of this invisible state via chemical shift ($\omega_A + \Delta\omega$), population (P_B), relaxation rate $\left(R_2^0 \approx R_{2B}^0\right)$ and rate of departure (k_B).

The simplest and most obvious parameter obtained from the dispersion curve is the relaxation rate in the absence of exchange R_2^0. This can be used to inform on ps-ns internal motions without being obscured by μs-ms exchange broadening and is discussed in the section on nuclear spin relaxation (section 3.6). This quantity also indicates the amount of exchange broadening, $R_{ex} = R_2^{Obs} - R_2^0 = R_2^{Obs}\left(\nu_{CPMG}^0\right) - R_2^{Obs}\left(\nu_{CPMG}^\infty\right)$, which can be estimated from the height of the dispersion curve (figure 14, c). R_{ex} is an attractive metric for quantifying μs-ms dynamics because it encapsulates the underlying process in a site-specific manner without requiring accurate details of molecular motion. Preliminary RD analyses typically display this parameter along the protein sequence or structure to identify regions of μs-ms flexibility and/or track its change with respect to experimental conditions (e.g., temperature, pH, amino acid sequence, ligand concentration). Although easily measured, the information contained in R_{ex} alone is limited since it is an oversimplification of the dynamic process. Specifically, it is affected by the magnitude of the chemical shift difference and the rates of interconversion and therefore cannot independently report on either quantity. Hence, the observed exchange broadening is generally the start of a more rigorous interpretation of the underlying μs-ms motions.

Detailed RD analysis can identify the nature of the dynamic structural change via the site-specific chemical shift difference between the A and B states, $\Delta\omega = \omega_A - \omega_B$. In general, only the magnitude $|\Delta\omega|$ is fit to the data whereas the sign (±) can be obtained by other methods [122,134]. To identify the nature of the minor state B, the site-specific $|\Delta\omega|$ values from RD are typically converted to ppm and compared against site-specific chemical shift differences, $\Delta\delta$, between those of the A state and a *candidate* structure representing the B state (e.g., a ligand-bound structure, a denatured structure – via pH, temperature or chaotropes). In this way, the chemical shifts of the candidate B state can be directly observed by selection of experimental conditions or calculated based on empirical or theoretical data. Importantly, correlation between site-specific $|\Delta\omega|$ from RD and $\Delta\delta$ from structural information validates the hypothesis that the minor state reported by RD resembles the structural candidate. This hypothesis is important to test because it can help identify the structural nature of the minor state conformer and therefore can address more general questions related to the biological functions of the exchange.

This approach has provided essential insights into the dihydrofolate reductase (DHFR) enzymatic cycle, which involves population of five ground-state structures to catalyze conversion of DHF to THF (figure 15). Remarkably, CPMG RD experiments indicate that each ground state in the cycle samples a structure similar to the adjacent state, suggesting that the motions present in the ground-state predispose the enzyme for the next catalytic step [120]. This hypothesis is rigorously validated via ($|\Delta\omega|$, $\Delta\delta$)-correlations since site-specific chemical shifts of the candidate B state (and hence $\Delta\delta$s) can be directly detected via heteronuclear correlation spectra for each structure in the cycle.

Generally, the structural features of the minor state are not well defined by conventional NMR methods, since they are better suited to characterizing the major state. However, in a

ground-breaking study, RD data were used to obtain a high-resolution structural model of an "invisible" minor state of the Abp1p SH3 domain [135]. This study applied previously demonstrated RD NMR methods to quantify residual dipolar couplings (RDCs) of a molecule undergoing chemical exchange [136]. A number of structural restraints for this minor state were obtained by performing a series of RD experiments to extract chemical shifts of backbone ^{15}N, ^{1}H^{N}, ^{13}C$^{\alpha}$ and ^{13}C' resonances, RDCs for bonds involving backbone atoms ^{1}H^{N}-^{15}N, ^{1}H$^{\alpha}$-^{13}C$^{\alpha}$ and ^{1}H^{N}-^{13}C', and residual chemical shift anisotropy for ^{13}C'. As a proof-of-principle study, the minor conformer selected was the ligand-bound form of Abp1p SH3 domain, which was populated to 5-10% by adding the corresponding mole-fraction of Ark1p peptide ligand. In this way, the structural metrics obtained indirectly via CPMG RD could be checked for accuracy by comparison with the data from the fully ligand-bound form. This study is groundbreaking because the parameters used to constrain the structural model were not observed directly but were instead identified via the ν_{CPMG}-dependent exchange-broadening of the directly-detected major state. Further studies report that side chain conformations can be probed in a similar manner [28,137-140].

In addition to providing information on the structure of the minor state via $\Delta\omega$, RD informs on the timescale of exchange via k_{ex}. This can be considered a metric for "flexibility" since it indicates how rapidly the alternate structure is sampled. For RNase A, RD analysis allowed its internal dynamics to be correlated to its catalytic turnover rate [141]. By utilizing aqueous solvents with varying proportions of D_2O, identical kinetic isotope effects were found on the rate of loop motion measured by CPMG RD (k_{ex}), and the rate of catalytic turnover measured by an RNA cleavage assay (k_{cat}). Remarkably, histidine 48 was found to have a role in modulating and coordinating catalytically productive motions in the enzyme despite its distance from the active site. This study exemplifies the connection between flexibility and function and identifies the importance of experimental studies that can identify such non-intuitive allosteric effects.

Although k_{ex} is informative, exchange kinetics are more completely described by the individual forward and reverse rates k_A and k_B that sum to k_{ex}. These two parameters and their dependence on experimental conditions characterize the "dynamic experience" of each structural probe and can help identify the "dynamic relationship" between a *pair* of structural probes. The three dynamic relationships summarized in table 1 are as follows. (i) If the pair of structural probes α and β report on the same physical process, their forward and reverse rates should be equal under all experimental conditions. That is, $k_A{}^{\alpha} = k_A{}^{\beta}$ and $k_B{}^{\alpha} = k_B{}^{\beta}$, denoted $(k_A, k_B)^{\alpha} = (k_A, k_B)^{\beta}$ and $\dfrac{\Delta k_{A,B}^{\alpha}}{\Delta Conditions} = \dfrac{\Delta k_{A,B}^{\beta}}{\Delta Conditions}$ where $\Delta Conditions$ refers to a change in experimental conditions such as temperature, pressure, ionic strength or pH. This situation may occur, for example, in hinged motion of a protein domain if each probe is near the hinge, like two observers on different sides of a see-saw. (ii) If each probe reports an independent process, or "mode", then there is no requirement that their rates or dependence upon conditions are related (though they could be). This may occur in two distant protein loops, each of which fluctuates with rates and energies characteristic of loops in general, though the motion of one has no direct effect upon the motion of the other. (iii) If the pair of probes report on two processes that are coupled (i.e., motion at site α directly affects motion at site β and vice-versa), then each process may occur with different rates but both should be sensitive to the same changes in conditions. That is, if motion at site α directly affects motion at site β then it will not be possible to change either of their rates independently. The magnitude of motional coupling lies along a continuum and therefore it can be difficult to define quantitatively (i.e., some motions are more coupled than others). Hence the significance of coupling should be considered in the context of function (e.g., allosteric communication via dynamics).

Such thorough analyses can yield powerful insights into protein dynamics, but not without certain limitations. It is possible that changes in experimental conditions may alter the dynamic relationship (e.g., loop-loop motions may be coupled at low temperature but be independent at high temperature). Furthermore, the observation that two probes exhibit the same exchange rates and sensitivity to conditions does not *necessarily* indicate they report on the same physical process (table 1). For example, they could report independent processes that coincidentally have the same dynamic experience, like the two loops described above in (ii). Furthermore, the parameters k_A and k_B do not identify synchrony of dynamic events nor the velocity of the transition from A→B or B→A. Instead, they simply quantify how often the transition occurs.

The notion of independent dynamic processes has been described for the protein NAD(P)H:flavin oxioreductase (FRE) bound with flavin adenine dinucleotide (FAD) [115]. By comparing k_A and k_B values for a number of probes, three groups within the protein were found to exhibit distinct dynamic motions with distinct biological implications (figure 16). This partitioning illustrates the complexity and heterogeneous nature of protein dynamics. Indeed, if a single protein can partition different regions of structure into different dynamic modes, it may be able to accomplish more unique functions (e.g., one site for binding and another for chemical transformation).

Provided temperature-dependent data on the rates of interconversion, additional energetic insights can be obtained. Arrhenius analysis quantifies the temperature dependence of exchange *rate constants* $\ln(k) = \ln(C) + \left(\dfrac{-E_A}{R}\right)\left(\dfrac{1}{T}\right)$ where $k = k_A$ (or k_B), C is the pre-exponential factor (the rate constant at infinite temperature from A→B (or B→A)), E_A is the activation energy ($\approx$ enthalpy) required to exchange A→B (or B→A), R is the gas constant and T is absolute temperature. Van't Hoff analysis quantifies the temperature dependence of exchanging *populations* via $\ln\left(\dfrac{k_A}{k_B}\right) = \dfrac{\Delta S_0}{R} + \left(\dfrac{\Delta H_0}{R}\right)\left(\dfrac{1}{T}\right)$ where ΔS_0 is the system entropy change from state A→B and ΔH_0 is the system enthalpy change from state A→B. Implementation of this approach is detailed in a study mapping the free energy landscape along the reaction coordinate of dihydrofolate reductase [117].

Accurate analysis of RD data may be hindered because there are often many sets of model parameters that fit the dispersion curve well [142,143]. This issue can be addressed by increasing the number of independent observations and/or decreasing the number of model parameters (i.e., maximizing the degrees of freedom $v = N_{obs} - N_{params}$, section A.1). Increasing independent observations is typically accomplished by recording data at multiple magnetic field strengths and/or using different types of magnetization (e.g., SQ, MQ, ZQ, DQ) [27,122]. The additional data are valuable because some model parameters are shared between the data sets (e.g., $|\Delta v|$ scales with B_0).

Decreasing the number of fitting parameters is often accomplished by assuming that sets of residues within the protein undergo concerted/global motion. Each motional mode within the protein may have a distinct set of (k_A, k_B, ΔH_0, ΔS_0, $E^A_{A \to B}$ and $E^A_{B \to A}$). That is, each probe in this region of structure alternates between its A and B state at the same rate (k) *and* this trend is maintained over a range of temperatures (van't Hoff and Arrhenius analyses of $K = k_A/k_B$ and k). Therefore, instead of assigning a unique (k_A, k_B) for each residue, a common value is assigned to a *group* of residues, thus sparing two parameters per residue included in the group.

Even when using such "global analysis" approaches in order to group independent motional modes, it is essential to rigorously explore the breadth of parameter-space with a defined

metric for fitting accuracy. This ensures that the best fit is obtained and assesses the possibility of alternate fitting solutions which may preclude further analysis. Regarding statistical model selection, it is generally true that more complex models (i.e., more parameters) simulate the data at least as well as their simpler counterparts. Statistical tests help determine whether the fit is sufficiently improved to justify use of the more complex model (section A.1) [144].

Experimentally, CPMG RD exchange rates are limited to $k_{ex} \approx$ 100-3,000 /sec, which is determined in part by the limits of applied CPMG frequency (i.e., how rapidly the spin-echo pulses can be applied). The lowest value of v_{CPMG} is achieved by using only one spin echo in the CPMG period. For proteins, this places a lower limit of around 25 Hz since transverse magnetization cannot "survive" a total CPMG time of greater than 20-50 ms. The upper limit of v_{CPMG} is typically around 1200 Hz due to hardware limitations of the RF probe and/ or significant sample heating [45,145,146]. Pulse imperfections may also yield spurious and/ or uninterpretable dispersions [147]. CPMG RD is a method undergoing active development, both in terms of its methodology and its breath of application.

3.5. Rotating Frame Relaxation Dispersion (RF RD) ($τ_{ex} \approx$ 20-100 μs; $k_{ex} \approx$ 10,000-50,000 / sec; intermediate-fast exchange $k_{ex} \geq Δv$)

Rotating frame relaxation dispersion (RF RD) can be used to study exchange events in the 20-100 μs time window [5,44,45,148]. Physical processes in this time window include motions of loops [141,149], side chains and occasionally, secondary structure elements. These may affect ligand binding and release, allostery [5] and the rate of catalytic turnover [141].

RF RD exploits the phenomenon of chemical exchange in the intermediate-fast regime where signals are only slightly broadened due to exchange ($k_{ex} \geq Δv$, figure 3). As described in section 3.6, exchange broadening R_{ex} can be attenuated by applying refocusing pulses at frequencies comparable to the total exchange rate k_{ex}; thus, CPMG RD reduces R_2 relaxation of transverse magnetization in the lab frame using spin-echo pulses in the range $v_{CPMG} \approx$ 25-1200 Hz. By analogy, RF RD reduces $R_{1\rho}$ relaxation of magnetization locked along the effective field in the rotating frame using spin-lock pulses in the range $\omega_{eff} \approx$ 1-50 kHz. In other words, CPMG RD can study ~ms exchange events and RF RD can study ~μs exchange events via the same principles.

The mechanism of spin-locking utilized by RF RD can be explained by first considering routine application of a radio-frequency (RF) pulse which has three primary characteristics: (1) carrier frequency ω_{RF}, (2) amplitude B_1 and (3) phase φ (figure 17). The carrier frequency ω_{RF} and amplitude B_1 determine *which* nuclei are affected by the pulse. The difference in nuclear precession frequency ω_0 and RF pulse frequency ω_{RF} is called the resonance offset $\Omega = \omega_0 - \omega_{RF}$. If the offset Ω is large relative to the precession rate from the RF pulse ω_1, it will not be affected by the pulse and is denoted "off-resonance" [2]. In practice, both RF frequency and amplitude are adjusted to affect the desired nuclei in the sample.

Two limiting cases are frequently encountered experimentally. (1) A "hard pulse" serves to manipulate magnetization using a defined precession rate, duration and orientation (e.g., 25 kHz for 10 μs (90°) along the x-axis, 25 kHz for 20 μs (180°) along the y-axis). In this case, the applied B_1 field is on-resonance and large relative to the resonances of interest ($\omega_1 \gg$

---

[2]Note that any NMR precession frequency can be expressed as a magnetic field strength applied perpendicular to the axis of precession for a given nucleus by use of its gyromagnetic ratio γ: static field $B_0 = -\omega_0 / \gamma$, RF field $B_1 = -\omega_1 / \gamma$ and offset field $-\Omega / \gamma$..

Ω) and therefore the effective field is tipped to an angle $\theta = tan^{-1}(\omega_1 / \Omega) \approx tan\text{-}1(\infty) = 90°$. In this case, during the RF pulse the magnetization precesses about B_{eff} at a rate

$\omega_{eff} = -\gamma B_{eff} = -\gamma \sqrt{(-\omega_1/\gamma)^2 + (-\Omega/\gamma)^2} \approx -\gamma \sqrt{(-\omega_1/\gamma)^2 + 0} = \omega_1$. (2) A weak and/or off-resonance pulse should not affect the magnetization. In this case, ($\omega_1 << \Omega$) and therefore the effective field is tipped to angle $\theta = tan^{-1}(\omega / \Omega) \approx tan^{-1}(0) = 0°$. The magnetization is not altered since B_{eff} is collinear with the main B_0 field. Therefore, in order to produce a B_{eff} at some non-trivial angle, the applied B_1 field must be greater than or equal to the offset field Ω / γ.

Magnetization can be locked along the direction of the effective field as long as the RF pulse is applied. In this rotating reference frame, relaxation of magnetization aligned with the effective field is a combination of R_1 and R_2 from the lab frame designated

$R_{1\rho} = 1/T_{1\rho} = R_1 cos^2(\theta) + (R_2^0 + R_{ex}) sin^2(\theta)$. The relaxation rate of magnetization perpendicular to the effective field is analogously designated $R_{2\rho}$. This can also be used to study dynamics [150] but in practice is much less common. In the presence of chemical exchange ($R_{ex} > 0$), $R_{1\rho}$ is increased because the nucleus spends time in different chemical environments during the spin-lock period of $R_{1\rho}$ relaxation. This affect can be attenuated with increasing effective field strength ω_{eff} by the same spin-echo principles outlined in the CPMG section (section 3.4). That is, as magnetization is "flipped" more frequently there is less time available to exchange to the alternate chemical shift. Unlike CPMG RD, the effective field strength can be increased in more than one way: (1) "near-" or "on-resonance" methods *fix* the RF carrier ω_{RF} in the center of the NMR spectrum (hence small site-specific Ω's). The effective field is increased simply by increasing ω_1 with a minimum value such that $\theta \geq 70°$ for each signal. (2) "off-resonance" methods can achieve larger effective fields by placing the RF carrier ω_{RF} far from the NMR signals of interest (hence large site-specific Ω's) and increase ω_{eff} by increasing ω_1 and/or Ω (via ω_{RF}) such that $\theta < 70°$ for each signal. In this context, the CPMG approach can be considered a low-power on-resonance rotating frame experiment with effective field strength $\omega_{eff} = \sqrt{48}\nu_{CPMG}$ in the limit of fast exchange [131]. To reiterate an important point, RF RD simply applies higher frequency effective fields by use of the spin-lock to study faster exchange kinetics than its CPMG counterpart. The remaining differences between these methods are simply due to the unique effects of the applying the refocusing pulse off-resonance.

For either on- or off-resonance approaches, the site-specific $R_{1\rho}$ is measured via loss of signal intensity during the relaxation delay for each value of effective field strength ω_{eff} (figure 18) . This may be measured in a two-point method like CPMG RD or more commonly using an independent time-series to fit an exponential decay function $I(t) = I_0 \cdot exp(-R_{1\rho}t)$. Because $R_{1\rho}$ is sensitive to R_{ex} and θ, and both are sensitive to ω_{eff}, the effects from reducing R_{ex} and altering θ are unfortunately convoluted. Therefore, the dispersion curve is most informative when displayed as $R_2^{Obs}(\omega_{eff})$ because this isolates the response from R_{ex}. This is done by using the relation $R_2^{Obs} = R_2^0 + R_{ex} = (R_{1\rho} - R_1 cos^2(\theta)) / sin^2(\theta)$ with known values of ω_{RF} and signal frequency ω_0 to calculate $\theta = tan^{-1}(\omega_1 / \Omega)$, where $\Omega = \omega_0 - \omega_{RF}$, and independently measuring the site-specific R_1 in the laboratory frame. It is also possible to measure $R_{1\rho} - R_1$ directly, thus obviating the need for an independent measure of R_1 [151].

Like CPMG RD, the relationship between R_2^{Obs} and the effective field strength ω_{eff} can be used to fit a model of exchange. For fast exchange between two states ($k_{ex} >> \Delta\nu$), this can

be expressed as $R_2^{Obs} = R_2^0 + R_{ex} = R_2^0 + \dfrac{P_A P_B \Delta\omega^2 k_{ex}}{k_{ex}^2 + \omega_{eff}^2} = R_2^0 + \dfrac{\phi_{ex} k_{ex}}{k_{ex}^2 + \omega_{eff}^2}$ with ω (rad/sec) = $2\pi \cdot \nu$(Hz)

(note this has a similar form to equation 2). More complex expressions have been derived and experimentally validated in the absence of fast exchange and even permit identification of the ± sign of $\Delta\omega$ [152-155]. Dispersion curves plot a metric for exchange broadening such as R_2^{Obs}, R_{ex} or $R_{1\rho}$ (which is less informative) as a function of a metric for field strength such as ω_{eff}, ω_{eff}^2, ω_1 (if Ω is fixed), Ω (if ω_1 is fixed) or θ.

Off-resonance RF RD has been used to study backbone amide and methyl side chain flexibility in the protein FKBP12 [156]. In addition to its isomerase activity, this regulatory protein functions to bind a variety of cellular targets in response to the drug FK506. In the absence of drug, the backbone and side chains report exchange at a rate of 8,000 /sec (figure 19). Upon binding FK506, there are coincident changes in both structure and dynamics of the protein that presumably enable binding of cellular targets. Details of the drug-induced changes in dynamics support a rare and interesting model in which the backbone becomes rigid at this timescale, while the side chain motions are enhanced in both frequency and prevalence throughout the structure. This result supports the hypothesis that promiscuous binding is enabled by increased flexibility of the side chains to compensate for the structurally-adjusted and rigidified backbone.

Analysis of RF RD can be limited because nearly all the measured exchange phenomena are in the fast regime ($k_{ex} >> \Delta v$). In this regime, the exchange populations and chemical shift differences become convoluted into a single variable, $\Phi_{ex} = P_A P_B \Delta\omega^2$, thereby limiting the interpretations of both P_A and $\Delta\omega$. In this case, the minimum chemical shift difference can estimated via $|\Delta\omega|_{min} = \sqrt{\phi_{ex}/max(P_A P_B)}$ with $max(P_A P_B) = max(P_A(1-P_A)) = (0.5)(0.5) = 0.25$ [156]. The temperature-dependence of Φ_{ex} can also help estimate $\Delta\omega$ value if $\Delta\omega$ is assumed to be constant [45]. Additionally, Φ_{ex} can be used directly to test whether the observed exchange corresponds to sampling a particular minor state (e.g., ligand bound, unfolded). Chemical shift differences between the observed state A and the candidate state B' can be obtained via standard NMR spectroscopy (CPMG RD section 3.4). By plotting site-specific Φ_{ex} as a function of $\Delta\delta^2$, a line can be fit to extract the slope $P_A P_B$ [123].

Experimentally, the high-power spin-lock fields used in RF RD may stress the NMR probe and/or produce undesirable heating of the sample [45,157]. Though not as commonly used as CPMG RD, RF RD is the method of choice for exchange processes in the μs time window. Dynamics at this timescale are being recognized as more pervasive that previously thought, and will likely garner increased attention as investigators fill the gaps in protein dynamic landscapes [158].

3.6. Nuclear Spin Relaxation (NSR) (ps-ns dynamics indirectly probed)

Nuclear spin relaxation (NSR) can be used to constrain a model of protein dynamics at the ps-ns timescale by measuring site-specific observables R_1, R_2 and the heteronuclear nuclear Overhauser effect *(hnNOE)* [44,159,160]. The physical processes in this time window include bond vibration and libration, side chain rotamer interconversion, random coil and loop motions and backbone torsion angle rotation. These motions have been implicated as important for enzyme catalysis, ligand specificity and affinity, allosteric effects [118,121], conformational entropy [29,31,161,162] and heat capacity [30,32,163].

Unlike the previously discussed methods, motions that affect NSR are not described as interconversion between two or more defined states. Instead, the site-specific dynamics are typically described within a single energy well by specifying the timescale of motion within the ps-ns time window and a metric for the amplitude of this motion via S^2, the square of the generalized order parameter. As mentioned in section 2, a set of excited nuclear spins will experience both longitudinal R_1 and transverse R_2 relaxation processes towards equilibrium.

Longitudinal (z) relaxation refers to "recovery" of net magnetization aligned with the applied field B_0. This is quantified by a time-dependent exponential restoration of intensity $I(t) = I(0) \cdot (1 - exp(-R_1 t))$ with rate constant $R_1 = 1/T_1$, which typically ranges from 0.5-5 Hz for large to small proteins. Transverse (x,y) relaxation refers to the loss of coherence of x,y-magnetization among the ensemble of spins. This is quantified by a time-dependent exponential reduction of intensity $I(t) = I(0) \cdot exp(-R_2 t)$ with rate constant $R_2 = 1/T_2$, which typically ranges from 5-50 Hz for small to large proteins. The *hnNOE* results from through-space magnetization transfer via dipolar coupling between different types of nuclei. Experimentally, this typically involves transfer from ^{1}H to a directly attached ^{15}N or [13]C "heteronucleus".

All NMR experiments alter the populations of nuclear quantum states and coherences among the population by applying time-dependent magnetic fields with frequencies denoted ω_{RF} (RF RD section 3.5). Particular values of ω_{RF} are selected to match the desired quantum transition based on the Larmor frequency ω_0. These values fall within the radio-frequency range of tens to hundreds of MHz depending on the type of nucleus and the static magnetic field strength B_0. The transitions are denoted "excitation" if they force the spin into a higher-energy "excited" state. However, an oscillating field could also induce "relaxation" if it forces the spin into a lower-energy "ground" state. Although relaxation transitions are generally not stimulated by experimental design, they continuously occur via oscillating fields resulting from random molecular motions in the ps-ns time window, corresponding to MHz-frequencies. Note that the rate of chemical exchange (~100-3,000 / sec) is too slow to produce Larmor frequency oscillating fields, but it nevertheless enhances R_2 by stochastically altering nuclear precession frequency and thus dephasing transverse magnetization (CPMG RD section 3.4). In general, there are three principle mechanisms that link ps-ns protein motions to these crucial MHz-frequency oscillating fields.

1. Chemical shift anisotropy (CSA) is the phenomenon that chemical shift, or equivalently local magnetic field, depends on the *orientation* of a bond vector relative to the static field B_0. That is, an amide nitrogen will experience a different local magnetic field (and thus different chemical shift) depending on the orientation of the N-H bond vector relative to the axis of the B_0 field. As the protein rotates relative to the B_0 field (tens of ns) and/or the bond vector rotates relative to the protein backbone (~ns-ps), the local magnetic field will change with time, thus producing a MHz-frequency oscillating field that can stimulate nuclear relaxation.

2. Dipolar coupling (DC) is a through-space interaction between pairs of nuclear spins that affects the magnetic field experienced by each spin. The magnitude of this interaction depends on both distance and orientation of the pair of nuclei relative to B_0. Since both inter-nuclear distance and orientation may change with time via ps-ns motions, DC will lead to local magnetic field oscillations with a MHz-frequency.

3. Quadrupolar interactions are possible between nuclei with a quadrupolar moment and an electric field gradient created by locally bonded electrons and/or ions. A non-zero quadrupolar moment occurs in nuclei with spin ≥ 1 such as ^{2}H, ^{14}N, [17]O and [19]F. This discussion is limited to the most common approach using side chain methyl groups $-C^1H_2{}^2H$. In this case, ^{2}H relaxation analyses are simplified because the quadrupolar interaction greatly exceeds both CSA and DC interactions (by 10-100 times). The magnitude of this interaction (and thus the ^{2}H relaxation rate) is sensitive to motions in the ps-ns time window via fluctuations of the local electric field gradient provided by the bonded carbon atom.

These three mechanisms qualitatively link ps-ns protein motions to the production of MHz-frequency oscillating fields. In order to quantitatively relate these oscillating fields to NMR

observables, it is necessary to quantify the ps-ns protein motions. This is accomplished by using an orientation correlation function $C(t)$, or equivalently a spectral density function $J(\omega)$ for each bond-vector. The orientation correlation function describes the time-dependence of bond reorientation and quantifies the rate at which the bond vector "forgets" its prior orientation and becomes randomized. In general, the correlation function is the dot product of the bond vector orientation $\vec{u}$ at time $t = 0$ with its value at a later time t given by $C(t) = \langle \vec{u}(0) \cdot \vec{u}(t) \rangle$. In the simple case of unrestricted molecular rotation and no internal motion, the correlation function exhibits exponential decay $C(t) = exp(t / \tau_m)$ where τ_m is the timescale of molecular rotation (tumbling in solution). Importantly, this function will decay to a minimum value after some time (~ns) reflecting the timescale of bond-vector reorientation. The correlation function can be Fourier transformed to recast this information as the "spectral density function" or "power spectrum" $J(\omega)$ which quantifies the amplitude of motion at any frequency ω. For proteins, both $C(t)$ and $J(\omega)$ will include effects from ~ns motion due to molecular rotation and potentially ~ps motion due to internal flexibility. Given the mechanisms for nuclear relaxation described above, a quantitative link between $J(\omega)$ and the NMR observables R_1, R_2 and $hnNOE$ (figure 20) are given by [44]:

$$R_1(X) = \frac{d_{HX}^2}{4}\left(J(\omega_H - \omega_X) + 3J(\omega_X) + 6J(\omega_H + \omega_X)\right) + c_X^2 J(\omega_X) \tag{4}$$

$$R_2(X) = \frac{d_{HX}^2}{8}\left(4J(0) + J(\omega_H - \omega_X) + 3J(\omega_X) + 6J(\omega_H) + 6J(\omega_H + \omega_X)\right) + \frac{c_X^2}{6}\left(4J(0) + 3J(\omega_X)\right) + R_{ex} \tag{5}$$

$$\{^1H\} - X hnNOE = 1 + \left(\frac{\gamma_H N}{\gamma_X R_1}\right)\frac{d_{HX}^2}{4}\left(6J(\omega_H + \omega_X) - J(\omega_H - \omega_X)\right) \tag{6}$$

$$R_1(^2H) = \frac{3}{16}\left[\frac{e^2 qQh}{2\pi}\right]^2 \left(J(\omega_D) + 4J(2\omega_D)\right) \tag{7}$$

$$R_{1\rho}(^2H) = \frac{1}{32}\left[\frac{e^2 qQh}{2\Pi}\right]\left(9J(0) + 15J(\omega_D) + 15J(6\omega_D)\right) \tag{8}$$

Where X = ^{13}C or ^{15}N attached to a ^1H nucleus, ω_X is the nuclear Larmor frequency, $d_{HX} = \left(\frac{\mu_0 h \gamma_H \gamma_X}{8\Pi^2}\right)\frac{1}{r_{HX}^3}$ is the dipolar interaction between X and its attached ^1H, μ_0 the permeability of free space, h is Planck's constant, γ is the nuclear gyromagnetic ratio, r_{HX} is the length of the H-X bond, $c_X = \Delta\sigma_X / \sqrt{3}$ is the CSA interaction, $\Delta\sigma_X$ the effective CSA for nucleus X, N is the number of ^1H atoms attached to nucleus X, e is the unit of electron charge, q is the magnitude of the electric field gradient and Q is the ^2H nuclear quadrupole moment.

Note that each observable is sensitive to a different combination of dynamics at the four NMR transition frequencies via $J(\omega_H)$, $J(\omega_X)$, $J(\omega_H + \omega_X)$ and $J(\omega_H - \omega_X)$, as well as inhomogeneity in the static field via $J(0)$. In general, relaxation is enhanced by increasing the amplitude of motion J *only* at these five frequencies whereas motions at other frequencies have no direct effect (except for chemical exchange R_{ex}).

The site-specific observables R_1, R_2 and *hnNOE* can be measured for ^{15}N, ^{13}C and ^{2}H sites on the protein backbone and side chains. Provided the appropriate isotope labeling scheme is used to simplify the relaxation processes, these experimental methods are straightforward [159,160]. Briefly, R_1 and R_2 data utilize a series of spectra that quantify the time-dependent buildup or decay of magnetization via R_1 or R_2 relaxation, respectively, and the *hnNOE* is obtained by comparing signal intensities in the presence and absence of dipolar coupling (figure 20, c). To better restrain fitting parameters, data are generally recorded at two magnetic field strengths.

Interpretation of nuclear relaxation rates is typically framed using one of at least four distinct approaches that fall along a continuum reflecting the degree of data processing and the degree of detail regarding the underlying physical processes. In general, less processing is more "pure" since it stays closer to the observed R_1, R_2 and *hnNOE* data, and it is more accurate since it requires fewer assumptions, but it is the more vague in assigning structural bases for the underlying protein dynamics. The four methods discussed here are (1) phenomenological interpretation of site-specific R_1, R_2 and *hnNOE*, each of which encapsulate different combinations of internal motions, (2) spectral density mapping, which reconstructs the site-specific $J(\omega)$ that quantify motions over a range of frequencies [164], (3) modelfree analysis, which assumes independence between internal motions and molecular tumbling [165] or (4) a specific model of internal motions that assumes details about the structure and interactions at the atomic level [166]. As with any of the above approaches, the goal is to understand protein function by quantifying the motions at each site in the protein. In what follows, each approach is discussed to identify its assets and limitations, and familiarize the reader with the type of analyses that are possible.

Phenomenological interpretation of R_1, R_2 and *hnNOE* requires no additional processing beyond measuring these site-specific observables. This analysis stays closest to the observed data, but consequently is the most limited toward assigning structural details. Typically, these data are shown along the sequence of the protein to identify regions of anomalous dynamic behavior. If the protein is internally rigid and tumbles isotropically, then the R_1, R_2 and *hnNOE* values will be the same at each site; therefore, values far from the average reflect site-specific internal motions and/or anisotropic molecular rotation. In general, for proteins R_1 ranges from 0.5-5 Hz and increases with faster tumbling and $J(\omega_X)$ (~50-200 MHz), and is decreased by ps-ns flexibility. R_2 ranges from 5-50 Hz and increases with slower tumbling, μs-ms chemical exchange R_{ex}, and inhomogenity in the static magnetic field $J(0)$. It decreases with ps-ns flexibility and is strongly affected by anisotropic rotation. The site-specific ratio R_1 / R_2 is constant for spherical molecules and therefore global structure-dependent differences can indicate anisotropic molecular rotation. The *hnNOE* ranges from −4 to 1 for {^{1}H}-^{15}N and from 1 to 3 for {^{1}H}-^{13}C and both are reduced in the presence of internal flexibility via $J(\omega H+\omega X) - J(\omega H-\omega X)$ [48]. Note that {^{1}H}-^{15}N *hnNOE* can fall below zero due to the negative sign of the ^{15}N gyromagnetic ratio γ.

Spectral density mapping and its more commonly used "reduced" counterpart [164] is only slightly removed from the observable data since R_1, R_2 and *hnNOE* are simply used to reconstruct each site-specific spectral density function $J(\omega)$. Much like the phenomenological approach, there is no underlying assumption about the nature of molecular motion. However, this approach is not used as frequently as modelfree analysis

(below), likely because it reflects an undesirable compromise between minimizing the processing of observables and maximizing the information on the underlying physical processes. That being said, $J(0.87\omega_H)$ is considered most diagnostic for ps-ns motions [164] and the modelfree parameters S^2 and τ_m can be estimated using $J(0)$, $J(\omega_H)$ and $J(\omega_X)$ [162,167]. Further details are reviewed elsewhere [159].

Modelfree analysis in its "extended" form [168] is the most commonly used approach for interpretation of R_1, R_2 and $hnNOE$ data. The approach assumes that internal motion is both independent of, and much faster than, molecular rotation (n.b., this is not always valid [169]). It is named "model free" because there is no *structural* model used to describe the nature of the motion, though it still is a model used to describe the NSR observables using four distinct types of parameters: (1) The rotational diffusion tensor D, which contains three unique elements D_{xx}, D_{yy} and D_{zz} to quantify the rate of molecular rotation about each of three axes. This can also be parameterized by a single ~ns correlation time τ_c or τ_m (figure 20, a). (2) The site-specific correlation time τ_e or τ_I quantifies the timescale of bond vector reorientation and can be partitioned into fast and slow components $\tau_{e,fast}$ and $\tau_{e,slow}$. (3) The site-specific squared order parameter S^2 (or O^2) quantifies the amplitude of internal motions that reorient the bond vector and can likewise be further partitioned into fast and slow components S^2_{fast} and S^2_{slow}. (4) The site-specific exchange broadening R_{ex} is the contribution to R_2 from µs-ms chemical exchange (section 2.2). The goal is to model the dynamics of each bond vector as simply as possible by prudently selecting the site-specific parameters (2), (3) and (4) [170] (model selection section A.1)

The order parameter S^2 garners the most attention in both modelfree analysis and studies of ps-ns motions in general. Its value is often considered to correspond to the amplitude of motion within a cone formed by the bond vector such that increasing rigidity corresponds to smaller cone angle θ (figure 20, d) [166]. Site-specific values of S^2 can range from 0 for a completely disordered bond-vector, to 1 for a completely rigid bond vector with uncertainties in fitted values derived from computer simulations [171]. As a note of caution, S2 may equal 0 even if the bond-vector is not completely disordered for at least two reasons: (1) if the bond vector is restricted to move within a cone with semi-angle equal to the "magic" angle 54.7°, or (2) if the bond vector is restricted to move in a hemisphere [165]. Empirically, S^2 values for backbone amide ^{15}N sites are found to be > 0.8 in the secondary structures and between 0.5 and 0.8 for loops, turns and termini [44]. The order parameters for side chain methyl ^{13}C sites can reflect flexibility of the entire side chain and are observed in the range between 0 and 1. In general, this flexibility is increased with side chain length, but correlations to structural location are less clear than for ^{15}N [160]. Additionally, flexibility about the threefold methyl symmetry axis can be quantified using ^{2}H relaxation and is denoted S^2_{axis}.

Order parameters are often mapped to the protein sequence or structure to identify local ps-ns rigidity. Likewise, changes in S^2 upon ligand binding (or similar) report on changes in ps-ns rigidity and can be quantitatively related to a change in conformational entropy ΔS_{conf} [31]. By measuring the temperature-dependence of this effect, the heat capacity C_p can also be estimated [32,163,172-174]. Unfortunately, these important thermodynamic interpretations of S^2 are complicated by several factors [159]. (1) The dynamics measured by S^2 may not report on independent degrees of freedom since some motions may be coupled, (2) internal degrees of freedom that do not reorient bond vectors will not be detected and (3) some degrees of freedom will simply not be detected due to lack of adequate structural probes. These problems have been addressed for the regulatory protein calmodulin (CaM) by assessing the correspondence between the change in order parameter ΔS^2 and the change in protein conformational entropy ΔS_{conf} upon binding six peptide targets with similar affinities but different binding entropies [29]. A linear correlation

between the change in S^2 of sidechain methyl groups (from NMR) and decomposed conformational entropy (from calorimetry) established an empirical relationship between the two parameters. The findings support the use of S^2 as a proxy for conformational entropy and underscore the importance of accounting for changes in protein flexibility when interpreting thermodynamics of interactions between proteins and their ligands.

Protein dynamics on the ps-ns timescale, as quantified by S^2, have also been shown to play a role in communicating allosteric effects via ΔS_{conf} [14,16,19]. For example, the catabolite activator protein (CAP) can bind DNA only when activated by the ligand cAMP [118]. Calorimetric experiments reveal that DNA binding to the WT CAP is driven by enthalpy ΔH but DNA binding to a mutant S26F CAP is driven by entropy ΔS. NMR experiments yielding backbone ^{15}N order parameters corroborate this finding by indicating the mutant CAP becomes *more* flexible upon DNA binding. Furthermore, these site-specific S^2 values reveal the increase in flexibility is most pronounced in the cAMP binding site, thus validating the allosteric linkage between the cAMP site and the DNA site (figure 21).

Modelfree parameters D, τ_e and R_{ex} can also provide valuable information about protein dynamics [159]. However, unlike S^2, these parameters are most often interpreted semi-quantitatively and may simply help direct more detailed studies (e.g., sites with $R_{ex} > 0$ can be further studied using relaxation dispersion methods discussed in sections 3.4 and 3.5).

The fourth distinct approach to interpretation of the NSR observables invokes a motional model with structural detail either using R_1, R_2 and *hnNOE* directly or using the results of modelfree analysis [159,166]. The most common model describes motion of the bond vector within a cone of angle θ defined by S^2 and diffusion time defined by τ_e (figure 20, d). Other models describe switching between distinct cones of motion or invoke a potential energy function for motion in a well. Another method, called slowly relaxing local structure (SRLS), is a powerful alternative to modelfree which does not require the assumption that internal and overall motions are independent [175].

As an experimental approach, nuclear spin relaxation is fundamentally restricted to detecting physical processes that alter the correlation function $C(t)$ for that bond vector. Therefore, rotation about the bond vector, translational diffusion and processes slower than molecular rotation ($\tau > \tau_m$) are all invisible to this approach [159]. In addition, the relative uncertainty in fitted order parameters S^2 may be both difficult to assess and prohibitively large [171]. Furthermore, this site-specific parameter simply encapsulates the underlying dynamic process but does not provide structural details (e.g., changes in atomic coordinates). This limitation can be mediated by use of molecular dynamics (MD) simulations to model ps-ns motions from which site-specific order parameters can be calculated [37,38].

3.7. Residual Dipolar Coupling (RDC) (ps-ms dynamics indirectly probed)

Residual dipolar couplings (RDCs) can be used to constrain a model of protein structure and dynamics in the ps-ms time window by combined analysis of site-specific coupling constants measured in an array of experimental conditions [176,177]. Dipolar coupling (DC) results from the mutual influence of magnetic dipole fields between two nuclei. This affects the local field at each nuclear center and therefore splits each NMR signal into two signals separated by a frequency equal to an effective coupling constant. This coupling occurs between all pairs of NMR-active nuclei and its magnitude depends on internuclear distance and orientation with respect to the static field B_0. Though the coupling is always "on", the signal splitting effect is nullified in solution where molecules rotate isotropically because all molecular orientations are sampled for the same amount of time. However, for molecules that are fixed in a solid state or rotate anisotropically, the signal splitting encapsulates orientation and dynamic information. Because splitting from DC can be relatively large

compared to the range of observed chemical shifts (up to 20 kHz for an NH pair), it is useful to attenuate it ~1,000 times to some non-zero "residual" value by imposing a small degree of preferential molecular orientation. Experimentally, this is achieved by use of a co-solvent that weakly aligns the protein with the magnetic field through steric or electrostatic effects; example alignment media include filamenous bacteriophage, bicelles, liquid crystals and polyacrylamide gels [178,179]. Interestingly, asymmetrically charged molecules with a non-zero magnetic susceptibility may exhibit anisotropic rotational diffusion even in the absence of an alignment medium [180,181]. Site-specific RDCs are then observed via a non-decoupled NMR spectrum that reveals a doublet for each signal separated by sum of the scalar and residual dipolar coupling constants, $J+RDC$ (figure 22, c).

The use of RDCs to study protein dynamics is somewhat analogous to the use of nuclear spin relaxation (NSR) (section 3.6). Site-specific NSR is sensitive to the rotation of the entire molecule and site-specific motion of the bond vector, whereas site-specific RDC is determined by the preferential orientation of the entire molecule and site-specific orientation and motion of the bond vector. In addition, NSR observables are only sensitive to motions faster than molecular tumbling (ns) because only these motions will produce MHz-oscillating magnetic fields required to stimulate spin relaxation. In contrast, since RDC splittings are observed via chemical shift, the upper limit on the time window is increased to that of chemical shift evolution (ms).

In order to extract dynamic information from RDCs one must deconvolute the time-dependent effect of the bond vector from the orientation-dependent effect of both the bond vector and the entire molecule. This is achieved by obtaining site-specific RDCs in at least five alignment media to yield at least five unique and orthogonal alignments relative to the magnetic field. These data are globally analyzed by (a) fitting a unique alignment tensor for each alignment medium, (b) fitting site-specific ps-ms order parameters S^2_{RDC} used for all alignment media and (c) obtaining site-specific bond vector orientations within the molecular frame (i.e., structural coordinates) used for all alignment media (figure 22). The structural coordinates can be used in at least four distinct ways: (1) a single structure refined by the RDC data [182], (2) a single structure which is not altered in the subsequent RDC analysis [183], (3), an ensemble of structures refined by the RDC data [184] or (4) an ensemble of structures from MD simulations which are not altered in the subsequent RDC analysis [185]. Importantly, all of these approaches assume that the choice of alignment medium only alters the preferential orientation of the molecule without affecting its internal structure and dynamics.

The site-specific order parameter S^2_{RDC} is the interpretable of interest and is defined in analogy to the modelfree order parameter from NSR denoted S^2_{NSR} or S^2_{LS} for Lipari and Szabo [165]. Like S^2_{NSR}, values range from 0 for a completely disordered bond vector to 1 for a completely rigid bond vector. The value can be used to determine an effective cone angle θ in which the bond vector may fluctuate (figure 22, d). Importantly, S^2_{RDC} reports on ps-ms motion whereas the S^2_{NSR} is limited to ps-ns or "sub-τ_c" motion, where $\tau_c = \tau_m$ is the correlation time for molecular rotation. Therefore, site-specific differences between S^2_{RDC} and S^2_{NSR} can identify ns-ms or "supra-τ_c" flexibility [184]. Currently this is the only NMR-based approach to access this time window, making RDCs essential for a comprehensive study of protein motions across all timescales (figure 5). In principle, $S^2_{RDC} \leq S^2_{NSR}$ for each site because expanding the time window from ps-ns to ps-ms may reveal previously undetected flexibility. Further generalizations are difficult because most research to date has focused on only a few proteins in order to fine-tune the methodology.

The protein ubiquitin has served as a test bed for many RDC based dynamics studies. In one such study, an "EROS" ensemble of ubiquitin structures was refined using NMR distance

restraints and orientational restraints from $H^N N$ RDCs in 36 alignment media, $H^N C'$ and NC' RDCs from 6 media and side chain methyl RDCs in 11 media (EROS = Ensemble Refinement with Orientational restraintS) [184]. Remarkably, this ps-ms ensemble encompasses the set of protein-bound ubiquitin structures observed via crystallography even though the crystal structures were not used in refinement. In contrast, an analogous ps-ns ensemble of ubiquitin structures did not encompass this variability. Indeed, comparison of site-specific order parameters S^2_{RDC} from the EROS ensemble with those from nuclear spin relaxation reveals ns-ms flexibility in loops, side chains and some parts of the backbone utilized for target binding (figure 23). It appears that the ns-ms motions uniquely probed by RDCs reflect a mechanism of conformational selection used by ubiquitin in recognition of a wide array of cellular partners (i.e., as opposed to a mechanism of induced fit). Furthermore, by using RDCs to refine a molecular ensemble, the structural nature of ps-ms motions are reported comprehensively via atomic coordinates. This study exemplifies the values of quantifying protein dynamics at all timescales and discusses additional important details regarding functional implications.

At this point, there is no consensus on the most accurate method for extracting dynamics from RDCs, and hence the EROS ensemble is just one of many approaches. Briefly, the ubiquitin RDC data set was also analyzed using accelerated molecular dynamics (AMD) to generate time-dependent ensemble of ubiquitin structures [185]. Yet another approach utilized unattenuated DCs from solid state NMR measurements of α-spectrin SH3 domain crystals [186]. In this crystalline case, relaxation effects from the large DC make the order parameter S^2_{DC} sensitive to motions only in the ps-μs time window (whereas S^2_{RDC} is sensitive to the larger ps-ms window).

Recent progress in DC includes methods for measuring ns-μs side chain dynamics [187], ms-sec dynamics [188,189] and revealing chemical exchange processes that are invisible in an isotropic medium [136]. By comparing observations among a range of overlapping time windows, motions within smaller time windows can be isolated. Overall, the DC methods for studying protein dynamics may seem intimidating and cumbersome since significant data and specialized samples are required, and subsequent analysis is technically complex (section A.1). However, as these methods continue to develop, their accessibility is also expected to improve.

3.8. Paramagnetic relaxation enhancement (PRE) ($\tau_{ex} \approx 10$ μs; $k_{ex} \approx 100,000$ /sec; fast exchange $k_{ex} \gg \Delta\Gamma$)

Paramagnetic relaxation enhancement (PRE) can be used to study protein dynamics at the μs timescale, typically for systems in fast exchange with a lowly populated species ($P_B \sim$ 0.1-10%) [190]. Therefore, this approach is best suited for studying non-specific interactions and encounter complexes between binding partners. PRE is a result of the magnetic dipole interaction between a nucleus and an unpaired electron. This nucleus-electron coupling will enhance site-specific nuclear relaxation rates R_1 and R_2 by an amount Γ_1 and Γ_2, respectively, in a distance-dependent manner within ~0.3-0.4 nm. The unpaired electron required for PRE is typically supplied by a paramagnetic ion which is either hydrated in the solvent or attached to a metal binding site in the protein. Protein-attachment can be accomplished using an endogenous metal-binding motif or by adding an exogenous metal-chelating tether. Importantly, the identity of the metal determines both qualitative and quantitative features of the interaction [190].

Site-specific PREs can be measured via the observed transverse relaxation rate $R_2^{Obs} = R_2^0 + R_{ex} + \Gamma_2$ in the presence ($\Gamma \geq 0$) and absence ($\Gamma = 0$) of the spin label using methods described previously (nuclear spin relaxation section 3.6). Characterization of an exchange process between states A and B requires a difference in PRE $\Delta\Gamma = |\Gamma_2^A - \Gamma_2^B|$ just like RD

methods require a difference in chemical shifts $\Delta\omega = |\omega^A - \omega^B|$. In the fast exchange regime, the observed PRE is the population-weighted average of the major and minor states: $\Gamma_{1,2}^{Obs} = P_A\Gamma_{1,2}^A + P_B\Gamma_{1,2}^B$. Typically, an experiment is designed such that the minor state B under investigation is closer to the paramagnetic probe than the major state A. Due to the strong distance-dependence of PRE, Γ_B can be much larger than Γ_A (by 10-10^5 Hz). Furthermore, if the B state population is too large, the effect from the A state is completely obscured. However, by selecting experimental conditions to limit P_B to around 0.1-10%, the effects from both A and B can be quantitatively studied to properly characterize the exchange phenomenon.

This method has been used to directly study nonspecific biomolecular interactions in their naturally dynamic mode [190]. Nonspecific interactions are essential to biology because they reduce the dimensionality of the diffusion/search problem. For example, a protein seeking a high-affinity DNA target sequence will require much less time on average if it slides in one dimension along the DNA non-specifically than if it diffuses in three dimensions through bulk solution. An analogous principle applies for protein-protein and protein-ligand interactions, in which formation of non-specific encounter complexes reduce the search-dimensionality from three to two or one.

This is exemplified by the proteins EIN and HPr which function in the bacterial phosphotransferase system by forming a $K_d \approx 10$ μM stereospecific complex. PRE experiments with spin-labeled HPr and ^{15}N-labeled EIN revealed a set of PRE contacts consistent with an ensemble of lowly-populated and fast-exchanging non-specific complexes in addition to the stable stereospecific complex [191] (figure 24). Structures of these encounter complexes were identified by computational docking methods [191] and later using enhanced sampling MD [192]. This analysis identified the structures of 10-20 complexes populated to a cumulative ~10%. The structural distribution of these species hints at how the proteins may encounter one another in solution prior to formation of the appropriate signaling complex. PRE has also been used to study open-close transitions in membrane proteins [193,194] and protein-DNA [195] interactions. This approach is limited because it is not always possible to extract detailed kinetic information from k_{ex} and P_B. However, this new method is developing rapidly and is essential for studying transient interactions at the molecular level.

4. Conclusion

Proteins can exhibit a wide range of dynamic behaviors that are important for their biological function. Protein dynamics must be defined, observed, understood and accurately predicted before they can be manipulated for novel designs and functions. Overall, protein dynamics are not yet well understood, and the field is still in the information-gathering stage. A wide array of powerful NMR-based methods are available for experimentally characterizing the dynamic behavior of proteins, and these will continue to be a workhorse for this important task. Recent developments in hardware, theory and application present an exciting trajectory. The task for NMR spectroscopists is in part to develop and improve tools for accessing new information in the full range of time windows. The task for biophysicists is in part to fill out the dynamic landscape for their proteins of interest and to continue to understand general features of protein dynamics. The task for biologists is in part to contextualize the general results towards understanding the extent to which dynamics are important for life.

Acknowledgments

Appendix

A.1. Scientific models and four steps to any experimental design and analysis

The goal of this section is to review complex analysis of experimental data by generalizing the process into a common model-based framework. This framework can be described by four steps: (1) acquire experimental result, (2) simulate experimental result using a model, (3) adjust model parameters to simulate the observed result as accurately as possible and (4) repeat steps (2)-(3) with a variety of candidate models to seek the most reasonable interpretation. Although this process is a general one, it is not always explicitly identified, especially for relatively simple and/or intuitive experiments. However, as experimental designs and analyses become increasingly complex, recognition of this framework can enhance the organization and efficacy of data analysis.

1. The acquisition of experimental results can be relatively simple or complex, the data can be few or many and can reflect many observables from one or more experimental instruments. Optimal selection of the number and type of data to acquire as well as the experimental conditions and instrumentation is a non-trivial process. One should consider the hypotheses to be addressed and the assets and limitations of the subsequent analysis. Although important, further details are beyond the scope of this discussion which focuses on the use of scientific models.

2. Experimental results are invariably interpreted with the help of a model which serves to both make predictions and simplify the observed phenomena. A good scientific model can be considered either a theory or hypothesis and exhibits the additional properties of being both testable and falsifiable. Example models include the two-state exchange of figure 3, a high-resolution structure of B-DNA, and may be as trivial as drawing a best fit line through observed (x,y) data (e.g., Newton's law $F = ma$).

3. To simulate the experimental result as accurately as possible, it is usually important to build variability into a model such that fine-tuning of its adjustable parameters can yield predictions to match a range of experimental observations. This fine-tuning can be accomplished by formulating a mathematical expression for the "goodness of fit" which yields a number that becomes smaller as the model more closely predicts the observed data. There are many ways to express this metric (e.g., PRE Q-factor, crystallographic R-factor) but the most common is the "chi-squared" value, $\chi^2 = \sum\limits_{i=1}^{N_{obs}} \left(\dfrac{Y_i^{Calc}\left(\overrightarrow{m}\right) - Y_i^{Obs}}{\sigma\left(Y_i^{Obs}\right)} \right)^2$, where N_{obs} is the total number of observations, $Y_i^{Calc}\left(\overrightarrow{m}\right)$ and Y_i^{Obs} are the calculated and observed values for the ith data point, respectively, with $\overrightarrow{m}$ representing the values of each adjustable model parameter and $\sigma\left(Y_i^{Obs}\right)$ is the experimental uncertainty in the ith observed data point. Thus, χ^2 is the square of the sum of the differences between the observed and predicted data after normalizing for noise in the data. The minimum value of zero is achieved when the model and observations agree exactly for all N_{obs} data points (though this rarely occurs).

To select an optimal set of values $\vec{m}$ for each adjustable model parameter, an iterative computational optimization process is typically used. At each step in the optimization, the values of $\vec{m}$ are discretely adjusted in an attempt to reduce χ^2 to a value smaller than at the previous step. This process is repeated until the changes in subsequent χ^2 values reach a plateau (n.b., unfortunately, some χ^2 surfaces contain multiple local minima and thus finding the "best fit" is non-trivial). At this point of minimum χ^2, the values of $\vec{m}$ reflect those which best simulate the observed data and the model can be used to make new predictions for cases which have not and/or cannot be observed.

4. Though a single optimized model is valuable, it is often important to compare a variety of candidate models to achieve the most reasonable compromise between model accuracy and simplicity / intuition. As explained in (3), accuracy can be quantified using χ^2 and optimized using an iterative computational process. In general, simplicity can be enhanced via prudent implementation of model parameters (i.e., by minimizing the number of parameters) and intuition can be enhanced by relinquishing both preconceived notions and details that are only incidental to the system under study. The relative complexity of a model can be expressed by its number of degrees of freedom $v = N_{obs} - N_{params}$ with N_{obs} the number of observations and N_{params} the number of model parameters. A value less than one precludes further analysis because there are not enough observations to define the model. In general, more complex models contain more parameters (smaller v) and they fit the data at least as well as their simpler counterparts $\left(\chi^2_{Complex} \leq \chi^2_{Simple} \right)$. Candidate models can be compared in many ways by use of common statistical metrics, including: (1) the "reduced chi-squared" metric $\chi^2_v = \chi^2 / (N_{Obs} - N_{Params}) = \chi^2/v$ which simply normalizes the accuracy of the model to its relative complexity and is best for smaller data sets [196], (2) the Akaike Information Criterion $AIC = \chi^2 + 2N_{Params}$ [197-199], which employs a linear penalty for increasing model complexity regardless of the number of observations, and (3) the Bayesian Information Criterion $BIC = \chi^2 + N_{Params} \ln(N_{Obs})$ [198-200], which accounts for the relative model complexity in a way that is appropriate for larger data sets [196,198]. The value of a particular metric is calculated for each candidate model and the most appropriate model can be identified as the one which minimizes the selected metric. That is, out of models M1, M2, M3, M4, etc., the statistically favored model has the smallest χ^2_v or AIC or BIC. Another common method, designated the F-test, uses the ratio of χ^2_v values from two different models to yield a statistical significance associated with a hypothetical improvement in fit [196]. This value is often compared to a threshold significance, or p-value (e.g., 0.05, 0.01).

Practically, χ^2_v values fall between one and ten with a value of one being optimal since the difference between each calculated and observed datum is equal to the experimental uncertainty. Values much less than one reflect an overestimation of the experimental uncertainties whereas values much greater than one reflect a poor model and/or poor fit and/or underestimation of the experimental uncertainty.

Further discussion of these and other tests are beyond the scope of this review [201], but their essence is consistent with the philosophy that scientists should seek to explain phenomena as simply as possible, but no simpler. Considering the four steps in this procedure have been introduced, the following two examples are discussed for clarification.

Simpler example: time-dependent protein folding monitored by RT-NMR

(i) Experimental data are signal intensities I_F from the folded state F acquired at N_{obs} time points: $I_F(t_1)$, $I_F(t_2)$, …, $I_F(t_{Nobs})$ (figure 7, b). (ii) One candidate model used to simulate the data describes two-state unimolecular folding U→F with the rate $d[F]/dt = [U]k = ([P]_{tot} - [F])k$ where k is the folding rate constant and $[P]_{tot}$ is the total protein concentration. This can be integrated to yield $[F](t) = [P]_{tot}(1 - \exp(-kt))$ and, because signal intensity scales with concentration, $I_F(t) = I_{max}(1 - \exp(-kt))$. (iii) To optimize this model, the two parameters I_{max} and k are selected such that the difference between the set of model-calculated $I_F(t)$ values and observed $I_F(t)$ values is minimized using the metric

$$\chi_v^2 = \frac{1}{v}\sum_{i=1}^{N_{obs}}\left(\frac{I_F^{Calc}\left(\bar{m},t_i\right) - I_F^{Obs}(t_i)}{\sigma\left(I_F^{Obs}(t_i)\right)}\right)^2$$

with $\bar{m} = (I_{mex.}, k)$ and $v = N_{obs} - N_{params} = N_{obs} - 2$. (iv) Other reasonable models should be considered to explain the observations. In this case, we may consider a mechanism of U↔I↔F, which invokes an intermediate state and therefore yields a different mathematical expression for the time-dependence of the signal intensity, $I_F(t)$, that utilizes more than two parameters. In the case of [73] this more complex model was not required because the U→F model adequately described the data. The optimized U→F model (mechanism) predicts the concentrations of folded and unfolded species at any point in time and validates the absence of an intermediate species in the folding pathway. In the case indicated above, site-specific values of k are roughly equal throughout the protein structure (figure 7, d), validating a model in which protein folding is a global concerted process.

More complex example: NSR and modelfree study of ps-ns protein dynamics

(i) Experimental data used in NSR studies are signal intensities which can be analyzed to obtain the interpretables R_1, R_2 and the *hnNOE* (section 3.6) [43,159]. The site-specific relaxation rates R_1 and R_2 are determined by fitting an exponential function to time-dependent signal intensities during a relaxation delay (n.b., this process resembles the simpler example discussed previously). The site-specific *hnNOE* is obtained more simply by comparing signal intensities from an NMR spectrum with and without dipolar magnetization transfer (figure 20, c). Because R_1, R_2 and *hnNOE* can be obtained for each of the N_{AA} NMR signals (e.g., amide resonances) for each magnetic field strength B_0, there are $N_{obs} = 3N_{AA}N_{B0}$ observations in total. (ii) One set of candidate models used to simulate these three site-specific observables are encompassed within the extended modelfree approach, which describes both molecular rotation and internal dynamics (section 3.6). The variable parameters for a relatively simple form of extended modelfree include the timescale τ_e and order parameter S^2 for each of N_{AA} observed NMR signals and the three elements of the rotational diffusion tensor D_{xx}, D_{yy} and D_{zz}. These $2N_{AA}+3$ model parameters can be used to calculate the site-specific spectral density function $J(\omega)$ and therefore site-specific R_1, R_2 and *hnNOE* values using equations (4), (5), and (6). (iii) To optimize this simple model, the values of these $2N_{AA}+3$ parameters are selected such that the difference between the set of model-calculated and observed R_1, R_2 and *hnNOE* values is minimized using the metric

$$\chi_v^2 = \frac{1}{v}\sum_{i=1}^{N_{obs}}\left(\left(\frac{R_{1,i}^{Calc}\left(\bar{m}\right) - R_{1,i}^{Obs}}{\sigma\left(R_{1,i}^{Obs}\right)}\right)^2 + \left(\frac{R_{2,i}^{Calc}\left(\bar{m}\right) - R_{2,i}^{Obs}}{\sigma\left(R_{2,i}^{Obs}\right)}\right)^2 + \left(\frac{hnNOE_i^{Calc}\left(\bar{m}\right) - hnNOE_i^{Obs}}{\sigma\left(hnNOE_i^{Obs}\right)}\right)^2\right)$$

with

$\bar{m} = \left(S_1^2, \tau_{e,1}, \ldots, S_{N_{AA}}^2, \tau_{e,N_{AA}}, D_{xx}, D_{yy}, D_{zz}\right)$ and $g = n = N_{obs} - N_{params} = 3N_{AA}N_{B0} - (2N_{AA}+3)$ and i iterates over each value of B_0 for each NMR resonance. Due to the complex mathematics required to predict these observables via the modelfree approach, optimization utilizes a sophisticated iterative computational procedure to avoid being "trapped" in a local

minimum of χ^2. (iv) Other reasonable models to consider include the various forms of the extended modelfree approach (section 3.6). Briefly, one of the more complex models partitions the internal motion into fast and slow components by adding one additional parameter per NMR resonance (e.g., amide group). In this case, the variable parameters are S^2_{fast}, S^2_{slow} and τ_e for each of the N_{AA} NMR resonances and the three elements of the rotational diffusion tensor D_{xx}, D_{yy} and D_{zz}. These $3N_{AA}+3$ model parameters require a different mathematical expression to calculate the site-specific $J(\omega)$, but use the same equations (4), (5) and (6) for subsequent calculation of R_1, R_2 and $hnNOE$. This model will likely predict the data at least as well as the simper form (i.e., smaller χ^2) because the additional parameter can capture more detailed site-specific features of the data. However, the degrees of freedom will decrease to $v = N_{obs} - N_{params} = 3N_{AA}N_{B0} - (3N_{AA}+3)$ therefore requiring data from at least two B_0 fields to maintain $v > 0$ for proper comparison to the simpler model. To determine whether site-specific internal motion is best described by one or two timescales, the site-specific values of χ^2_v can be compared between the simpler and more complex models. In either case, the final model predicts a timescale of internal motion and the degree of order of the bond vector. This approach has significant predictive power because these quantities could not be measured directly.

In conclusion, many current biophysical analyses utilize a wide variety of independent data acquired under many experimental conditions (e.g., temperature, pressure, pH, ionic strength, ligand concentrations, magnetic field strength). The use of these additional independent data exploits the power of this framework by helping to formulate a model that is accurate under a wide array of conditions thereby enhancing its predictive power. Despite the appeal of this approach, it is valuable to consider the cautionary dictum of statistician George P. Box, "all models are wrong but some models are useful" [144]. This is an important reminder that all models have limitations, and that beyond these limits they fail to be useful for understanding and predicting phenomena. Furthermore, irrational attachment to an attractive but inappropriate model may hinder scientific progress. Although some models are more useful than others, there is no "perfect" model and furthermore any model at its *absolute best* is simply (i) consistent with all observed data (i.e. testable predictions are validated experimentally), (ii) consistent within itself (i.e., logically sound), and (iii) generates meaningful predictions for cases which have not and/or cannot be observed.

Abbreviations

NMR	nuclear magnetic resonance
s	second
ms	millisecond (10^{-3} s)
μs	microsecond (10^{-6} s)
ns	nanosecond (10^{-9} s)
ps	picosecond (10^{-12} s)
k_{ex}	chemical exchange rate constant
τ_{ex}	chemical exchange timescale ($= 1 / k_{ex}$)
R_{ex}	transverse relaxation rate constant due to chemical exchange
RDC	residual dipolar coupling
RT NMR	real time NMR
NSR	nuclear spin relaxation

RF RD	rotating frame relaxation dispersion
CPMG RD	Carr-Purcell Meiboom-Gill relaxation dispersion
EXSY	EXchange SpectroscopY
PRE	paramagnetic relaxation enhancement
S^2	square of the generalized modelfree order parameter

References

[1]. Henzler-Wildman K, Kern D. Dynamic personalities of proteins. Nature. 2007:964–972. [PubMed: 18075575]

[2]. Boehr DD, Dyson HJ, Wright PE. An nmr perspective on enzyme dynamics. Chem. Rev. 2006:3055–3079. [PubMed: 16895318]

[3]. Kamerzell TJ, Middaugh CR. The complex inter-relationships between protein flexibility and stability. J Pharm Sci. 2008:3494–3517. [PubMed: 18186490]

[4]. Namanja AT, Wang XJ, Xu B, Mercedes-Camacho AY, Wilson BD, Wilson KA, Etzkorn FA, Peng JW. Toward flexibility-activity relationships by nmr spectroscopy: dynamics of pin1 ligands. J. Am. Chem. Soc. 2010:5607–5609. [PubMed: 20356313]

[5]. Loria JP, Berlow RB, Watt ED. Characterization of enzyme motions by solution nmr relaxation dispersion. Acc. Chem. Res. 2008:214–221. [PubMed: 18281945]

[6]. Smock RG, Gierasch LM. Sending signals dynamically. Science. 2009:198–203. [PubMed: 19359576]

[7]. Neudecker P, Lundström P, Kay LE. Relaxation dispersion nmr spectroscopy as a tool for detailed studies of protein folding. Biophys. J. 2009:2045–2054. [PubMed: 19289032]

[8]. Dyson HJ, Wright PE. Elucidation of the protein folding landscape by nmr. Meth. Enzymol. 2005:299–321. [PubMed: 15808225]

[9]. Tycko R. Molecular structure of amyloid fibrils: insights from solid-state nmr. Q. Rev. Biophys. 2006:1–55. [PubMed: 16772049]

[10]. Boehr DD, Nussinov R, Wright PE. The role of dynamic conformational ensembles in biomolecular recognition. Nat. Chem. Biol. 2009:789–796. [PubMed: 19841628]

[11]. Boehr DD, Wright PE. Biochemistry. how do proteins interact? Science. 2008:1429–1430. [PubMed: 18556537]

[12]. Tompa P, Fuxreiter M. Fuzzy complexes: polymorphism and structural disorder in protein-protein interactions. Trends Biochem. Sci. 2008:2–8. [PubMed: 18054235]

[13]. Csermely P, Palotai R, Nussinov R. Induced fit, conformational selection and independent dynamic segments: an extended view of binding events. Trends Biochem. Sci. 2010

[14]. Kern D, Zuiderweg ERP. The role of dynamics in allosteric regulation. Curr. Opin. Struct. Biol. 2003:748–757. [PubMed: 14675554]

[15]. Cooper A, Dryden DT. Allostery without conformational change. a plausible model. Eur. Biophys. J. 1984:103–109. [PubMed: 6544679]

[16]. Tsai C, Del Sol A, Nussinov R. Protein allostery, signal transmission and dynamics: a classification scheme of allosteric mechanisms. Mol Biosyst. 2009:207–216. [PubMed: 19225609]

[17]. Tsai C, del Sol A, Nussinov R. Allostery: absence of a change in shape does not imply that allostery is not at play. J. Mol. Biol. 2008:1–11. [PubMed: 18353365]

[18]. Gunasekaran K, Ma B, Nussinov R. Is allostery an intrinsic property of all dynamic proteins? Proteins. 2004:433–443. [PubMed: 15382234]

[19]. Cui Q, Karplus M. Allostery and cooperativity revisited. Protein Sci. 2008:1295–1307. [PubMed: 18560010]

[20]. Laskowski RA, Gerick F, Thornton JM. The structural basis of allosteric regulation in proteins. FEBS Lett. 2009:1692–1698. [PubMed: 19303011]

[21]. Peng JW. Communication breakdown: protein dynamics and drug design. Structure. 2009:319–320. [PubMed: 19278644]

[22]. Lee GM, Craik CS. Trapping moving targets with small molecules. Science. 2009:213–215. [PubMed: 19359579]

[23]. Pellecchia M, Bertini I, Cowburn D, Dalvit C, Giralt E, Jahnke W, James TL, Homans SW, Kessler H, Luchinat C, Meyer B, Oschkinat H, Peng J, Schwalbe H, Siegal G. Perspectives on nmr in drug discovery: a technique comes of age. Nat Rev Drug Discov. 2008:738–745. [PubMed: 19172689]

[24]. Khersonsky O, Tawfik DS. Enzyme promiscuity: a mechanistic and evolutionary perspective. Annu. Rev. Biochem. 2010:471–505. [PubMed: 20235827]

[25]. Valente AP, Miyamoto CA, Almeida FCL. Implications of protein conformational diversity for binding and development of new biological active compounds. Curr Med Chem. 2006:3697–3703. [PubMed: 17168731]

[26]. Tokuriki N, Tawfik DS. Protein dynamism and evolvability. Science. 2009:203–207. [PubMed: 19359577]

[27]. Korzhnev DM, Kay LE. Probing invisible, low-populated states of protein molecules by relaxation dispersion nmr spectroscopy: an application to protein folding. Acc. Chem. Res. 2008:442–451. [PubMed: 18275162]

[28]. Baldwin AJ, Kay LE. Nmr spectroscopy brings invisible protein states into focus. Nat. Chem. Biol. 2009:808–814. [PubMed: 19841630]

[29]. Marlow MS, Dogan J, Frederick KK, Valentine KG, Wand AJ. The role of conformational entropy in molecular recognition by calmodulin. Nat. Chem. Biol. 2010:352–358. [PubMed: 20383153]

[30]. Lee AL, Wand AJ. Microscopic origins of entropy, heat capacity and the glass transition in proteins. Nature. 2001:501–504. [PubMed: 11373686]

[31]. Yang D, Kay LE. Contributions to conformational entropy arising from bond vector fluctuations measured from nmr-derived order parameters: application to protein folding. J. Mol. Biol. 1996:369–382. [PubMed: 8913313]

[32]. Yang D, Mok YK, Forman-Kay JD, Farrow NA, Kay LE. Contributions to protein entropy and heat capacity from bond vector motions measured by nmr spin relaxation. J. Mol. Biol. 1997:790–804. [PubMed: 9368658]

[33]. Adcock SA, McCammon JA. Molecular dynamics: survey of methods for simulating the activity of proteins. Chem. Rev. 2006:1589–1615. [PubMed: 16683746]

[34]. Bahar I, Lezon TR, Bakan A, Shrivastava IH. Normal mode analysis of biomolecular structures: functional mechanisms of membrane proteins. Chem. Rev. 2010:1463–1497. [PubMed: 19785456]

[35]. Bahar I, Rader AJ. Coarse-grained normal mode analysis in structural biology. Curr. Opin. Struct. Biol. 2005:586–592. [PubMed: 16143512]

[36]. Trbovic N, Kim B, Friesner RA, Palmer AG 3. Structural analysis of protein dynamics by md simulations and nmr spin-relaxation. Proteins. 2008:684–694. [PubMed: 17975832]

[37]. Caballero-Manrique E, Bray JK, Deutschman WA, Dahlquist FW, Guenza MG. A theory of protein dynamics to predict nmr relaxation. Biophys. J. 2007:4128–4140. [PubMed: 17766356]

[38]. Nodet G, Abergel D. An overview of recent developments in the interpretation and prediction of fast internal protein dynamics. Eur. Biophys. J. 2007:985–993. [PubMed: 17562038]

[39]. Berjanskii M, Wishart DS. Nmr: prediction of protein flexibility. Nat Protoc. 2006:683–688. [PubMed: 17406296]

[40]. Trott O, Siggers K, Rost B, Palmer AG 3. Protein conformational flexibility prediction using machine learning. J. Magn. Reson. 2008:37–47. [PubMed: 18313957]

[41]. Palmer AG 3. Nmr probes of molecular dynamics: overview and comparison with other techniques. Annu Rev Biophys Biomol Struct. 2001:129–155. [PubMed: 11340055]

[42]. Mittermaier AK, Kay LE. Observing biological dynamics at atomic resolution using nmr. Trends Biochem. Sci. 2009:601–611. [PubMed: 19846313]

[43]. Rule, GS.; Hitchens, KT. Fundamentals of protein nmr spectroscopy. Springer; Dordrecht, The Netherlands: 2006.

[44]. Kempf JG, Loria JP. Protein dynamics from solution nmr: theory and applications. Cell Biochem. Biophys. 2003:187–211. [PubMed: 12625627]

[45]. Palmer AG 3, Kroenke CD, Loria JP. Nuclear magnetic resonance methods for quantifying microsecond-to-millisecond motions in biological macromolecules. Meth. Enzymol. 2001:204–238. [PubMed: 11462813]

[46]. Palmer AG 3, Grey MJ, Wang C. Solution nmr spin relaxation methods for characterizing chemical exchange in high-molecular-weight systems. Meth. Enzymol. 2005:430–465. [PubMed: 15808232]

[47]. Cavanagh, J.; Fairbrother, WJ.; Palmer, AGI.; Rance, M.; Skelton, NJ. Protein nmr spectroscopy. Elsevier; Burlington, MA, USA: 2007.

[48]. Levitt, MH. Spin dynamics: basics of nuclear magnetic resonance. John Wiley & Sons Ltd.; West Sussex, England: 2001.

[49]. Bloch F. Nuclear induction. Phys. Rev. 1946:460–474.

[50]. Bloch F, Hansen WW, Packard M. The nuclear induction experiment. Phys. Rev. 1946:474–485.

[51]. Purcell E, Torrey H, Pound R. Resonance absorption by nuclear magnetic moments in a solid. Phys. Rev. 1946:37–38.

[52]. Ohki S, Kainosho M. Stable isotope labeling methods for protein nmr spectroscopy. Prog Nucl Magn Reson Spectros. 2008:208–226.

[53]. Ruschak AM, Kay LE. Methyl groups as probes of supra-molecular structure, dynamics and function. J. Biomol. NMR. 2010:75–87. [PubMed: 19784810]

[54]. Wishart DS, Case DA. Use of chemical shifts in macromolecular structure determination. Meth. Enzymol. 2001:3–34. [PubMed: 11460554]

[55]. Mulder FAA, Filatov M. Nmr chemical shift data and ab initio shielding calculations: emerging tools for protein structure determination. Chem Soc Rev. 2010:578–590. [PubMed: 20111782]

[56]. Shen Y, Lange O, Delaglio F, Rossi P, Aramini JM, Liu G, Eletsky A, Wu Y, Singarapu KK, Lemak A, Ignatchenko A, Arrowsmith CH, Szyperski T, Montelione GT, Baker D, Bax A. Consistent blind protein structure generation from nmr chemical shift data. Proc. Natl. Acad. Sci. U.S.A. 2008:4685–4690. [PubMed: 18326625]

[57]. Wishart DS, Nip AM. Protein chemical shift analysis: a practical guide. Biochem. Cell Biol. 1998:153–163. [PubMed: 9923684]

[58]. Abergel D, Palmer AG. Approximate solutions of the bloch-mcconnell equations for two-site chemical exchange. Chemphyschem. 2004:787–793. [PubMed: 15253305]

[59]. McConnell H. Reaction rates by nuclear magnetic resonance. J Chem Phys. 1958:430–431.

[60]. Felli IC, Brutscher B. Recent advances in solution nmr: fast methods and heteronuclear direct detection. Chemphyschem. 2009:1356–1368. [PubMed: 19462391]

[61]. Foster MP, McElroy CA, Amero CD. Solution nmr of large molecules and assemblies. Biochemistry. 2007:331–340. [PubMed: 17209543]

[62]. Skrisovska L, Schubert M, Allain FH. Recent advances in segmental isotope labeling of proteins: nmr applications to large proteins and glycoproteins. J. Biomol. NMR. 2010:51–65. [PubMed: 19690964]

[63]. Zeeb M, Balbach J. Protein folding studied by real-time nmr spectroscopy. Methods. 2004:65–74. [PubMed: 15283916]

[64]. Harper SM, Neil LC, Day IJ, Hore PJ, Gardner KH. Conformational changes in a photosensory lov domain monitored by time-resolved nmr spectroscopy. J. Am. Chem. Soc. 2004:3390–3391. [PubMed: 15025443]

[65]. Corazza A, Rennella E, Schanda P, Mimmi MC, Cutuil T, Raimondi S, Giorgetti S, Fogolari F, Viglino P, Frydman L, Gal M, Bellotti V, Brutscher B, Esposito G. Native-unlike long-lived intermediates along the folding pathway of the amyloidogenic protein beta2-microglobulin revealed by real-time two-dimensional nmr. J. Biol. Chem. 2010:5827–5835. [PubMed: 20028983]

[66]. Malmodin D, Billeter M. Multiway decomposition of nmr spectra with coupled evolution periods. J. Am. Chem. Soc. 2005:13486–13487. [PubMed: 16190698]

[67]. Malmodin D, Billeter M. Signal identification in nmr spectra with coupled evolution periods. J. Magn. Reson. 2005:47–53. [PubMed: 15972264]

[68]. Frydman L, Scherf T, Lupulescu A. The acquisition of multidimensional nmr spectra within a single scan. Proc. Natl. Acad. Sci. U.S.A. 2002:15858–15862. [PubMed: 12461169]

[69]. Schanda P, Brutscher B. Very fast two-dimensional nmr spectroscopy for real-time investigation of dynamic events in proteins on the time scale of seconds. J. Am. Chem. Soc. 2005:8014–8015. [PubMed: 15926816]

[70]. Schanda P, Kupce E, Brutscher B. Sofast-hmqc experiments for recording two-dimensional heteronuclear correlation spectra of proteins within a few seconds. J. Biomol. NMR. 2005:199–211. [PubMed: 16341750]

[71]. Pervushin K, Vögeli B, Eletsky A. Longitudinal (1)h relaxation optimization in trosy nmr spectroscopy. J. Am. Chem. Soc. 2002:12898–12902. [PubMed: 12392438]

[72]. Gal M, Kern T, Schanda P, Frydman L, Brutscher B. An improved ultrafast 2d nmr experiment: towards atom-resolved real-time studies of protein kinetics at multi-hz rates. J. Biomol. NMR. 2009:1–10. [PubMed: 18982409]

[73]. Schanda P, Forge V, Brutscher B. Protein folding and unfolding studied at atomic resolution by fast two-dimensional nmr spectroscopy. Proc. Natl. Acad. Sci. U.S.A. 2007:11257–11262. [PubMed: 17592113]

[74]. Arrington CB, Robertson AD. Kinetics and thermodynamics of conformational equilibria in native proteins by hydrogen exchange. Meth. Enzymol. 2000:104–124. [PubMed: 10944749]

[75]. Bai Y, Englander JJ, Mayne L, Milne JS, Englander SW. Thermodynamic parameters from hydrogen exchange measurements. Meth. Enzymol. 1995:344–356. [PubMed: 8538461]

[76]. Hvidt A, Nielsen SO. Hydrogen exchange in proteins. Adv. Protein Chem. 1966:287–386. [PubMed: 5333290]

[77]. Bai Y, Milne JS, Mayne L, Englander SW. Primary structure effects on peptide group hydrogen exchange. Proteins. 1993:75–86. [PubMed: 8234246]

[78]. Bradbury JH, Crompton MW, Teh JS. Nuclear-magnetic-resonance study of the histidine residues of s-peptide and s-protein and kinetics of 1h-2h exchange of ribonuclease a. Eur. J. Biochem. 1977:411–422. [PubMed: 23288]

[79]. Markley JL. Correlation proton magnetic resonance studies at 250 mhz of bovine pancreatic ribonuclease. i. reinvestigation of the histidine peak assignments. Biochemistry. 1975:3546–3554. [PubMed: 240382]

[80]. Lee S, Mahler B, Toward J, Jones B, Wyatt K, Dong L, Wistow G, Wu Z. A single destabilizing mutation (f9s) promotes concerted unfolding of an entire globular domain in gammas-crystallin. J. Mol. Biol. 2010:320–330. [PubMed: 20382156]

[81]. Bai Y. Protein folding pathways studied by pulsed- and native-state hydrogen exchange. Chem. Rev. 2006:1757–1768. [PubMed: 16683753]

[82]. Jeener J, Meier B, Bachmann P, Ernst R. Investigation of exchange processes by 2-dimensional nmr-spectroscopy. J Chem Phys. 1979:4546–4553.

[83]. Religa TL, Sprangers R, Kay LE. Dynamic regulation of archaeal proteasome gate opening as studied by trosy nmr. Science. 2010:98–102. [PubMed: 20360109]

[84]. Key J, Scheuermann TH, Anderson PC, Daggett V, Gardner KH. Principles of ligand binding within a completely buried cavity in hif2alpha pas-b. J. Am. Chem. Soc. 2009:17647–17654. [PubMed: 19950993]

[85]. Demers J, Mittermaier A. Binding mechanism of an sh3 domain studied by nmr and itc. J. Am. Chem. Soc. 2009:4355–4367. [PubMed: 19267471]

[86]. Sahu D, Clore GM, Iwahara J. Trosy-based z-exchange spectroscopy: application to the determination of the activation energy for intermolecular protein translocation between specific sites on different dna molecules. J. Am. Chem. Soc. 2007:13232–13237. [PubMed: 17918842]

[87]. Doucleff M, Clore GM. Global jumping and domain-specific intersegment transfer between dna cognate sites of the multidomain transcription factor oct-1. Proc. Natl. Acad. Sci. U.S.A. 2008:13871–13876. [PubMed: 18772384]

[88]. Sprangers R, Gribun A, Hwang PM, Houry WA, Kay LE. Quantitative nmr spectroscopy of supramolecular complexes: dynamic side pores in clpp are important for product release. Proc. Natl. Acad. Sci. U.S.A. 2005:16678–16683. [PubMed: 16263929]

[89]. Nikolaev Y, Pervushin K. Nmr spin state exchange spectroscopy reveals equilibrium of two distinct conformations of leucine zipper gcn4 in solution. J. Am. Chem. Soc. 2007:6461–6469. [PubMed: 17469817]

[90]. Kuloğlu ES, McCaslin DR, Markley JL, Volkman BF. Structural rearrangement of human lymphotactin, a c chemokine, under physiological solution conditions. J. Biol. Chem. 2002:17863–17870. [PubMed: 11889129]

[91]. Sarkar P, Reichman C, Saleh T, Birge RB, Kalodimos CG. Proline cis-trans isomerization controls autoinhibition of a signaling protein. Mol. Cell. 2007:413–426. [PubMed: 17289588]

[92]. Fraser JS, Clarkson MW, Degnan SC, Erion R, Kern D, Alber T. Hidden alternative structures of proline isomerase essential for catalysis. Nature. 2009:669–673. [PubMed: 19956261]

[93]. Falzone CJ, Wright PE, Benkovic SJ. Dynamics of a flexible loop in dihydrofolate reductase from escherichia coli and its implication for catalysis. Biochemistry. 1994:439–442. [PubMed: 8286374]

[94]. Pervushin K, Riek R, Wider G, Wüthrich K. Attenuated t2 relaxation by mutual cancellation of dipole-dipole coupling and chemical shift anisotropy indicates an avenue to nmr structures of very large biological macromolecules in solution. Proc. Natl. Acad. Sci. U.S.A. 1997:12366–12371. [PubMed: 9356455]

[95]. Gemmecker G, Jahnke W, Kessler H. Measurement of fast proton exchange rates in isotopically labeled compounds. J. Am. Chem. Soc. 1993:11620–11621.

[96]. Böckmann A, Penin F, Guittet E. Rapid estimation of relative amide proton exchange rates of 15 n-labelled proteins by a straightforward water selective noesy-hsqc experiment. FEBS Lett. 1996:191–195.

[97]. Mori S, Abeygunawardana C, van Zijl PC, Berg JM. Water exchange filter with improved sensitivity (wex ii) to study solvent-exchangeable protons. application to the consensus zinc finger peptide cp-1. J Magn Reson B. 1996:96–101. [PubMed: 8556240]

[98]. Hwang TL, van Zijl PC, Mori S. Accurate quantitation of water-amide proton exchange rates using the phase-modulated clean chemical exchange (cleanex-pm) approach with a fast-hsqc (fhsqc) detection scheme. J. Biomol. NMR. 1998:221–226. [PubMed: 9679296]

[99]. Brand T, Cabrita EJ, Morris GA, Günther R, Hofmann H, Berger S. Residue-specific nh exchange rates studied by nmr diffusion experiments. J. Magn. Reson. 2007:97–104. [PubMed: 17475526]

[100]. Chevelkov V, Xue Y, Rao DK, Forman-Kay JD, Skrynnikov NR. 15n h/d-solexsy experiment for accurate measurement of amide solvent exchange rates: application to denatured drkn sh3. J. Biomol. NMR. 2010:227–244. [PubMed: 20195703]

[101]. Hofmann H, Weininger U, Löw C, Golbik RP, Balbach J, Ulbrich-Hofmann R. Fast amide proton exchange reveals close relation between native-state dynamics and unfolding kinetics. J. Am. Chem. Soc. 2009:140–146. [PubMed: 19061322]

[102]. Li Y, Palmer AG 3. Trosy-selected zz-exchange experiment for characterizing slow chemical exchange in large proteins. J. Biomol. NMR. 2009:357–360. [PubMed: 19890725]

[103]. Doucet N, Watt ED, Loria JP. The flexibility of a distant loop modulates active site motion and product release in ribonuclease a. Biochemistry. 2009:7160–7168. [PubMed: 19588901]

[104]. Mittag T, Schaffhausen B, Günther UL. Tracing kinetic intermediates during ligand binding. J. Am. Chem. Soc. 2004:9017–9023. [PubMed: 15264834]

[105]. Beach H, Cole R, Gill ML, Loria JP. Conservation of mus-ms enzyme motions in the apo- and substrate-mimicked state. J. Am. Chem. Soc. 2005:9167–9176. [PubMed: 15969595]

[106]. Kern D, Eisenmesser EZ, Wolf-Watz M. Enzyme dynamics during catalysis measured by nmr spectroscopy. Meth. Enzymol. 2005:507–524. [PubMed: 15808235]

[107]. Lineshapekin. http://lineshapekin.net/

[108]. Günther UL, Schaffhausen B. Nmrkin: simulating line shapes from two-dimensional spectra of proteins upon ligand binding. J. Biomol. NMR. 2002:201–209.

[109]. Meiboom S, Gill D. Modified spin-echo method for measuring nuclear relaxation times. Re. Sci. Instrum. 1963:688–691.

[110]. Luz Z, Meiboom S. Nuclear magnetic resonance study of protolysis of trimethylammonium ion in aqueous solution - order of reaction with respect to solvent. J. Chem. Phys. 1963:366–370.

[111]. Carr H, Purcell E. Effects of diffusion on free precession in nuclear magnetic resonance experiments. Phys. Rev. 1954:630–638.

[112]. Loria J, Rance M, Palmer A. A relaxation-compensated carr-purcell-meiboom-gill sequence for characterizing chemical exchange by nmr spectroscopy. J Amer Chem Soc. 1999:2331–2332.

[113]. Ishima R, Torchia DA. Extending the range of amide proton relaxation dispersion experiments in proteins using a constant-time relaxation-compensated cpmg approach. J. Biomol. NMR. 2003:243–248. [PubMed: 12652136]

[114]. Lundström P, Vallurupalli P, Hansen DF, Kay LE. Isotope labeling methods for studies of excited protein states by relaxation dispersion nmr spectroscopy. Nat Protoc. 2009:1641–1648. [PubMed: 19876024]

[115]. Vallurupalli P, Kay LE. Complementarity of ensemble and single-molecule measures of protein motion: a relaxation dispersion nmr study of an enzyme complex. Proc. Natl. Acad. Sci. U.S.A. 2006:11910–11915. [PubMed: 16880391]

[116]. Kovrigin EL, Loria JP. Enzyme dynamics along the reaction coordinate: critical role of a conserved residue. Biochemistry. 2006:2636–2647. [PubMed: 16489757]

[117]. Boehr DD, McElheny D, Dyson HJ, Wright PE. Millisecond timescale fluctuations in dihydrofolate reductase are exquisitely sensitive to the bound ligands. Proc. Natl. Acad. Sci. U.S.A. 2010:1373–1378. [PubMed: 20080605]

[118]. Tzeng S, Kalodimos CG. Dynamic activation of an allosteric regulatory protein. Nature. 2009:368–372. [PubMed: 19924217]

[119]. Brüschweiler S, Schanda P, Kloiber K, Brutscher B, Kontaxis G, Konrat R, Tollinger M. Direct observation of the dynamic process underlying allosteric signal transmission. J. Am. Chem. Soc. 2009:3063–3068. [PubMed: 19203263]

[120]. Boehr DD, McElheny D, Dyson HJ, Wright PE. The dynamic energy landscape of dihydrofolate reductase catalysis. Science. 2006:1638–1642. [PubMed: 16973882]

[121]. Popovych N, Sun S, Ebright RH, Kalodimos CG. Dynamically driven protein allostery. Nat. Struct. Mol. Biol. 2006:831–838. [PubMed: 16906160]

[122]. Korzhnev DM, Neudecker P, Mittermaier A, Orekhov VY, Kay LE. Multiple-site exchange in proteins studied with a suite of six nmr relaxation dispersion experiments: an application to the folding of a fyn sh3 domain mutant. J. Am. Chem. Soc. 2005:15602–15611. [PubMed: 16262426]

[123]. Farber P, Darmawan H, Sprules T, Mittermaier A. Analyzing protein folding cooperativity by differential scanning calorimetry and nmr spectroscopy. J. Am. Chem. Soc. 2010:6214–6222. [PubMed: 20377225]

[124]. Schanda P, Brutscher B, Konrat R, Tollinger M. Folding of the kix domain: characterization of the equilibrium analog of a folding intermediate using 15n/13c relaxation dispersion and fast 1h/2h amide exchange nmr spectroscopy. J. Mol. Biol. 2008:726–741. [PubMed: 18565542]

[125]. Sugase K, Dyson HJ, Wright PE. Mechanism of coupled folding and binding of an intrinsically disordered protein. Nature. 2007:1021–1025. [PubMed: 17522630]

[126]. Wolf-Watz M, Thai V, Henzler-Wildman K, Hadjipavlou G, Eisenmesser EZ, Kern D. Linkage between dynamics and catalysis in a thermophilic-mesophilic enzyme pair. Nat. Struct. Mol. Biol. 2004:945–949. [PubMed: 15334070]

[127]. Eisenmesser EZ, Bosco DA, Akke M, Kern D. Enzyme dynamics during catalysis. Science. 2002:1520–1523. [PubMed: 11859194]

[128]. Labeikovsky W, Eisenmesser EZ, Bosco DA, Kern D. Structure and dynamics of pin1 during catalysis by nmr. J. Mol. Biol. 2007:1370–1381. [PubMed: 17316687]

[129]. Eisenmesser EZ, Millet O, Labeikovsky W, Korzhnev DM, Wolf-Watz M, Bosco DA, Skalicky JJ, Kay LE, Kern D. Intrinsic dynamics of an enzyme underlies catalysis. Nature. 2005:117–121. [PubMed: 16267559]

[130]. Carver JP, Richards RE. General 2-site solution for chemical exchange produced depenence of t2 upon carr-purcell pulse separation. J. Magn. Reson. 1972:89.

[131]. Ishima R, Torchia DA. Estimating the time scale of chemical exchange of proteins from measurements of transverse relaxation rates in solution. J. Biomol. NMR. 1999:369–372. [PubMed: 10526408]

[132]. Millet O, Loria JP, Kroenke CD, Pons M, Palmer AG. The static magnetic field dependence of chemical exchange linebroadening defines the nmr chemical shift time scale. J. Am. Chem. Soc. 2000:2867–2877.

[133]. Ishima R, Torchia DA. Accuracy of optimized chemical-exchange parameters derived by fitting cpmg r2 dispersion profiles when r2(0a) not = r2(0b). J. Biomol. NMR. 2006:209–219. [PubMed: 16645811]

[134]. Skrynnikov NR, Dahlquist FW, Kay LE. Reconstructing nmr spectra of "invisible" excited protein states using hsqc and hmqc experiments. J. Am. Chem. Soc. 2002:12352–12360. [PubMed: 12371879]

[135]. Vallurupalli P, Hansen DF, Kay LE. Structures of invisible, excited protein states by relaxation dispersion nmr spectroscopy. Proc. Natl. Acad. Sci. U.S.A. 2008:11766–11771. [PubMed: 18701719]

[136]. Igumenova TI, Brath U, Akke M, Palmer AG 3. Characterization of chemical exchange using residual dipolar coupling. J. Am. Chem. Soc. 2007:13396–13397. [PubMed: 17929930]

[137]. Hansen DF, Neudecker P, Vallurupalli P, Mulder FAA, Kay LE. Determination of leu side-chain conformations in excited protein states by nmr relaxation dispersion. J. Am. Chem. Soc. 2010:42–43. [PubMed: 20000605]

[138]. Hansen DF, Neudecker P, Kay LE. Determination of isoleucine side-chain conformations in ground and excited states of proteins from chemical shifts. J. Am. Chem. Soc. 2010:7589–7591. [PubMed: 20465253]

[139]. Lundström P, Lin H, Kay LE. Measuring 13cbeta chemical shifts of invisible excited states in proteins by relaxation dispersion nmr spectroscopy. J. Biomol. NMR. 2009:139–155. [PubMed: 19448976]

[140]. Baldwin AJ, Hansen DF, Vallurupalli P, Kay LE. Measurement of methyl axis orientations in invisible, excited states of proteins by relaxation dispersion nmr spectroscopy. J. Am. Chem. Soc. 2009:11939–11948. [PubMed: 19627152]

[141]. Watt ED, Shimada H, Kovrigin EL, Loria JP. The mechanism of rate-limiting motions in enzyme function. Proc. Natl. Acad. Sci. U.S.A. 2007:11981–11986. [PubMed: 17615241]

[142]. Kovrigin EL, Kempf JG, Grey MJ, Loria JP. Faithful estimation of dynamics parameters from cpmg relaxation dispersion measurements. J. Magn. Reson. 2006:93–104. [PubMed: 16458551]

[143]. Ishima R, Torchia DA. Error estimation and global fitting in transverse-relaxation dispersion experiments to determine chemical-exchange parameters. J. Biomol. NMR. 2005:41–54. [PubMed: 16041482]

[144]. Box, GE.; Hunter, SJ.; Hunger, WG. Statistics for experimenters. John Wiley & Sons, Inc.; Hoboken, New Jersey: 2005.

[145]. Myint W, Gong Q, Ishima R. Practical aspects of 15n cpmg transverse relaxation experiments for proteins in solution. Concepts in Magnetic Resonance Part A. 2009:63–75.

[146]. Yip GNB, Zuiderweg ERP. Improvement of duty-cycle heating compensation in nmr spin relaxation experiments. J. Magn. Reson. 2005:171–178. [PubMed: 16009587]

[147]. Yip GNB, Zuiderweg ERP. A phase cycle scheme that significantly suppresses offset-dependent artifacts in the r2-cpmg 15n relaxation experiment. J. Magn. Reson. 2004:25–36. [PubMed: 15504678]

[148]. Palmer AG 3, Massi F. Characterization of the dynamics of biomacromolecules using rotating-frame spin relaxation nmr spectroscopy. Chem. Rev. 2006:1700–1719. [PubMed: 16683750]

[149]. Wang Y, Berlow RB, Loria JP. Role of loop-loop interactions in coordinating motions and enzymatic function in triosephosphate isomerase. Biochemistry. 2009:4548–4556. [PubMed: 19348462]

[150]. Michaeli S, Sorce DJ, Idiyatullin D, Ugurbil K, Garwood M. Transverse relaxation in the rotating frame induced by chemical exchange. J. Magn. Reson. 2004:293–299. [PubMed: 15261625]

[151]. Akke M, Palmer A. Monitoring macromolecular motions on microsecond to millisecond time scales by r(1)rho-r(1) constant relaxation time nmr spectroscopy. J Amer Chem Soc. 1996:911–912.

[152]. Trott O, Palmer AG. R-1 rho relaxation outside of the fast-exchange limit. J. Magn. Reson. 2002:157–160. [PubMed: 11820837]

[153]. Trott O. An average-magnetization analysis of r-1 rho relaxation outside of the fast exchange. Mol Phys. 2003:753–763.

[154]. Abergel D, Palmer AG. On the use of the stochastic liouville equation in nuclear magnetic resonance: application to r-1 rho relaxation in the presence of exchange. Concepts Magn Reson Part A. 2003:134–148.

[155]. Korzhnev DM, Orekhov VY, Dahlquist FW, Kay LE. Off-resonance r1rho relaxation outside of the fast exchange limit: an experimental study of a cavity mutant of t4 lysozyme. J. Biomol. NMR. 2003:39–48. [PubMed: 12766401]

[156]. Brath U, Akke M. Differential responses of the backbone and side-chain conformational dynamics in fkbp12 upon binding the transition-state analog fk506: implications for transition-state stabilization and target protein recognition. J. Mol. Biol. 2009:233–244. [PubMed: 19361439]

[157]. Wimmer R, Wider G. Real-time imaging of the spatial distribution of rf-heating in nmr samples during broadband decoupling. J. Magn. Reson. 2007:184–192. [PubMed: 17507272]

[158]. Hansen DF, Feng H, Zhou Z, Bai Y, Kay LE. Selective characterization of microsecond motions in proteins by nmr relaxation. J. Am. Chem. Soc. 2009:16257–16265. [PubMed: 19842628]

[159]. Jarymowycz VA, Stone MJ. Fast time scale dynamics of protein backbones: nmr relaxation methods, applications, and functional consequences. Chem. Rev. 2006:1624–1671. [PubMed: 16683748]

[160]. Igumenova TI, Frederick KK, Wand AJ. Characterization of the fast dynamics of protein amino acid side chains using nmr relaxation in solution. Chem. Rev. 2006:1672–1699. [PubMed: 16683749]

[161]. Trbovic N, Cho J, Abel R, Friesner RA, Rance M, Palmer AG 3. Protein side-chain dynamics and residual conformational entropy. J. Am. Chem. Soc. 2009:615–622. [PubMed: 19105660]

[162]. Bracken C, Carr PA, Cavanagh J, Palmer AG 3. Temperature dependence of intramolecular dynamics of the basic leucine zipper of gcn4: implications for the entropy of association with dna. J. Mol. Biol. 1999:2133–2146. [PubMed: 9925790]

[163]. Kovrigin EL, Cole R, Loria JP. Temperature dependence of the backbone dynamics of ribonuclease a in the ground state and bound to the inhibitor 5′-phosphothymidine (3′-5′)pyrophosphate adenosine 3′-phosphate. Biochemistry. 2003:5279–5291. [PubMed: 12731869]

[164]. Farrow NA, Zhang O, Szabo A, Torchia DA, Kay LE. Spectral density function mapping using 15n relaxation data exclusively. J. Biomol. NMR. 1995:153–162. [PubMed: 8589604]

[165]. Lipari G, Szabo A. Model-free approach to the interpretation of nuclear magnetic resonance relaxation in macromolecules. 1. theory and range of validity. J. Am. Chem. Soc. 1982:4546–4559.

[166]. Daragan VA, Mayo KH. Motional model analyses of protein and peptide dynamics using 13c and 15n nmr relaxation. Prog. NMR Spec. 1997:63–105.

[167]. Lefevre JF, Dayie KT, Peng JW, Wagner G. Internal mobility in the partially folded dna binding and dimerization domains of gal4: nmr analysis of the n-h spectral density functions. Biochemistry. 1996:2674–2686. [PubMed: 8611573]

[168]. Clore GM, Szabo A, Bax A, Kay LE, Driscoll PC, Gronenborn AM. Deviations from the simple 2-parameter model-free approach to the interpretation of n-15 nuclear magnetic-relaxation of proteins. J. Am. Chem. Soc. 1990:4989–4991.

[169]. Chen K, Tjandra N. Extended model free approach to analyze correlation functions of multidomain proteins in the presence of motional coupling. J. Am. Chem. Soc. 2008:12745–12751. [PubMed: 18761455]

[170]. Mandel AM, Akke M, Palmer AG 3. Backbone dynamics of escherichia coli ribonuclease hi: correlations with structure and function in an active enzyme. J. Mol. Biol. 1995:144–163. [PubMed: 7531772]

[171]. Jin D, Andrec M, Montelione GT, Levy RM. Propagation of experimental uncertainties using the lipari-szabo model-free analysis of protein dynamics. J. Biomol. NMR. 1998:471–492. [PubMed: 9862126]

[172]. Massi F, Palmer AG 3. Temperature dependence of nmr order parameters and protein dynamics. J. Am. Chem. Soc. 2003:11158–11159. [PubMed: 16220912]

[173]. Vugmeyster L, Trott O, McKnight CJ, Raleigh DP, Palmer AG 3. Temperature-dependent dynamics of the villin headpiece helical subdomain, an unusually small thermostable protein. J. Mol. Biol. 2002:841–854. [PubMed: 12095260]

[174]. Mandel AM, Akke M, Palmer AG 3. Dynamics of ribonuclease h: temperature dependence of motions on multiple time scales. Biochemistry. 1996:16009–16023. [PubMed: 8973171]

[175]. Meirovitch E, Shapiro YE, Polimeno A, Freed JH. Structural dynamics of bio-macromolecules by nmr: the slowly relaxing local structure approach. Progress in Nuclear Magnetic Resonance Spectroscopy. 2010:360–405. [PubMed: 20625480]

[176]. Lakomek N, Lange OF, Walter KFA, Farès C, Egger D, Lunkenheimer P, Meiler J, Grubmüller H, Becker S, de Groot BL, Griesinger C. Residual dipolar couplings as a tool to study molecular recognition of ubiquitin. Biochem. Soc. Trans. 2008:1433–1437. [PubMed: 19021570]

[177]. Tolman JR, Ruan K. Nmr residual dipolar couplings as probes of biomolecular dynamics. Chem. Rev. 2006:1720–1736. [PubMed: 16683751]

[178]. Tolman JR. A novel approach to the retrieval of structural and dynamic information from residual dipolar couplings using several oriented media in biomolecular nmr spectroscopy. J. Am. Chem. Soc. 2002:12020–12030. [PubMed: 12358549]

[179]. Bax A. Weak alignment offers new nmr opportunities to study protein structure and dynamics. Protein Sci. 2003:1–16. [PubMed: 12493823]

[180]. Tjandra N, Omichinski JG, Gronenborn AM, Clore GM, Bax A. Use of dipolar 1h-15n and 1h-13c couplings in the structure determination of magnetically oriented macromolecules in solution. Nat. Struct. Biol. 1997:732–738. [PubMed: 9303001]

[181]. Prestegard JH, al-Hashimi HM, Tolman JR. Nmr structures of biomolecules using field oriented media and residual dipolar couplings. Q. Rev. Biophys. 2000:371–424. [PubMed: 11233409]

[182]. Lakomek N, Walter KFA, Farès C, Lange OF, de Groot BL, Grubmüller H, Brüschweiler R, Munk A, Becker S, Meiler J, Griesinger C. Self-consistent residual dipolar coupling based model-free analysis for the robust determination of nanosecond to microsecond protein dynamics. J. Biomol. NMR. 2008:139–155. [PubMed: 18523727]

[183]. Meiler J, Prompers JJ, Peti W, Griesinger C, Brüschweiler R. Model-free approach to the dynamic interpretation of residual dipolar couplings in globular proteins. J. Am. Chem. Soc. 2001:6098–6107. [PubMed: 11414844]

[184]. Lange OF, Lakomek N, Farès C, Schröder GF, Walter KFA, Becker S, Meiler J, Grubmüller H, Griesinger C, de Groot BL. Recognition dynamics up to microseconds revealed from an rdc-derived ubiquitin ensemble in solution. Science. 2008:1471–1475. [PubMed: 18556554]

[185]. Markwick PRL, Bouvignies G, Salmon L, McCammon JA, Nilges M, Blackledge M. Toward a unified representation of protein structural dynamics in solution. J. Am. Chem. Soc. 2009:16968–16975. [PubMed: 19919148]

[186]. Chevelkov V, Xue Y, Linser R, Skrynnikov NR, Reif B. Comparison of solid-state dipolar couplings and solution relaxation data provides insight into protein backbone dynamics. J. Am. Chem. Soc. 2010:5015–5017. [PubMed: 20297847]

[187]. Farès C, Lakomek N, Walter KFA, Frank BTC, Meiler J, Becker S, Griesinger C. Accessing ns-micros side chain dynamics in ubiquitin with methyl rdcs. J. Biomol. NMR. 2009:23–44. [PubMed: 19652920]

[188]. Li W, McDermott AE. Characterization of slow conformational dynamics in solids: dipolar codex. J. Biomol. NMR. 2009:227–232. [PubMed: 19662335]

[189]. Krushelnitsky A, deAzevedo E, Linser R, Reif B, Saalwächter K, Reichert D. Direct observation of millisecond to second motions in proteins by dipolar codex nmr spectroscopy. J. Am. Chem. Soc. 2009:12097–12099. [PubMed: 19673476]

[190]. Clore GM, Iwahara J. Theory, practice, and applications of paramagnetic relaxation enhancement for the characterization of transient low-population states of biological macromolecules and their complexes. Chem. Rev. 2009:4108–4139. [PubMed: 19522502]

[191]. Tang C, Iwahara J, Clore GM. Visualization of transient encounter complexes in protein-protein association. Nature. 2006:383–386. [PubMed: 17051159]

[192]. Kim YC, Tang C, Clore GM, Hummer G. Replica exchange simulations of transient encounter complexes in protein-protein association. Proc. Natl. Acad. Sci. U.S.A. 2008:12855–12860. [PubMed: 18728193]

[193]. Bermejo GA, Strub M, Ho C, Tjandra N. Ligand-free open-closed transitions of periplasmic binding proteins: the case of glutamine-binding protein. Biochemistry. 2010:1893–1902. [PubMed: 20141110]

[194]. Tang C, Schwieters CD, Clore GM. Open-to-closed transition in apo maltose-binding protein observed by paramagnetic nmr. Nature. 2007:1078–1082. [PubMed: 17960247]

[195]. Iwahara J, Schwieters CD, Clore GM. Characterization of nonspecific protein-dna interactions by 1h paramagnetic relaxation enhancement. J. Am. Chem. Soc. 2004:12800–12808. [PubMed: 15469275]

[196]. Jaqaman K, Danuser G. Linking data to models: data regression. Nat. Rev. Mol. Cell Biol. 2006:813–819. [PubMed: 17006434]

[197]. Akaike H. A new look at the statistical identification model. IEEE Trans Auto Control. 1974:716–723.

[198]. Chen J, Brooks CL 3, Wright PE. Model-free analysis of protein dynamics: assessment of accuracy and model selection protocols based on molecular dynamics simulation. J. Biomol. NMR. 2004:243–257. [PubMed: 15213423]

[199]. Kullback S, Leibler RA. On information and sufficiency. The Annals of Mathematical Statistics. 1951:79–86.

[200]. Schwarz G. Estimating the dimension of a model. The Annals of Statistics. 1978:461–464.

[201]. Myung JI. Evaluation and comparison of computational models. Meth Enzymology. 2009:287–304.

[202]. Chang S, Tjandra N. Temperature dependence of protein backbone motion from carbonyl 13c and amide 15n nmr relaxation. J. Magn. Reson. 2005:43–53. [PubMed: 15809171]
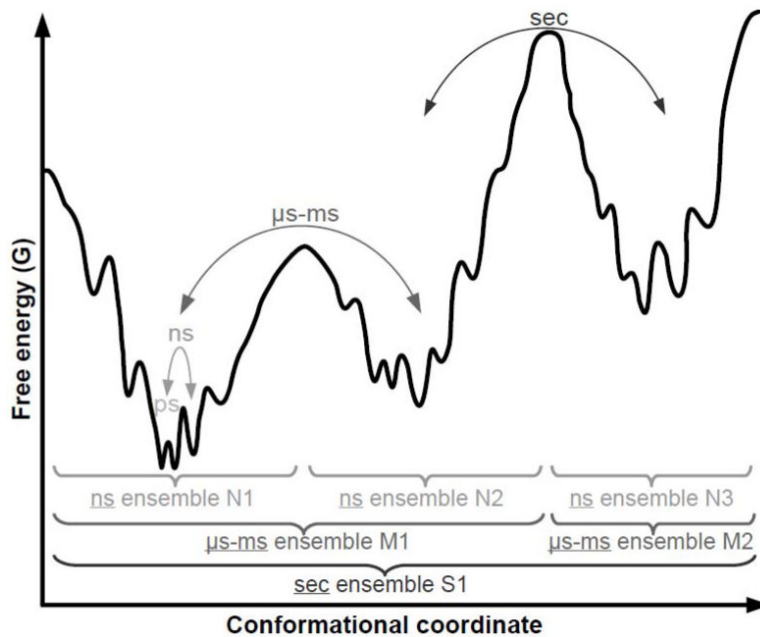
Figure 1.
Proteins sample a range of thermodynamically accessible conformations within a hierarchy of timescales owing to their intrinsic flexibility. The ~20 minima correspond to defined states with finite populations. The population of each state is determined by its relative free energy, while interconversion rates are determined by inter-state energy barriers. An ensemble of states comprises all the individual states within its defined time window. Although these time windows are best understood to lie along a continuum, they have been grouped into ps, ns, µs-ms and sec for clarity. To describe the "structure" of a protein it is important to recognize that its conformation will be time-averaged within the time window and ensemble-averaged within the set of molecules under observation. Note that the shape of this landscape is unique for each protein and may change with conditions (e.g., temperature, pressure, pH, ionic strength, ligand binding).
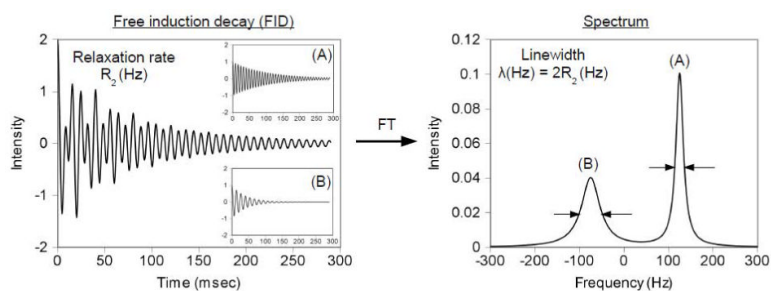
Figure 2.
The free induction decay (FID) is the fundamental NMR observable and encapsulates the individual signals from each site-specific probe in the molecule. This time-dependent signal **(left)** is Fourier transformed into the frequency domain **(right)** for quantification of the three primary NMR observables: (1) frequency (or chemical shift δ) is the position of the peak in the spectrum and reports on local chemical environment, (2) intensity I can be quantified by peak height or peak area and reports on populations and (3) linewidth λ is the full peak width at half maximum height and reports on local dynamics via the relaxation rate $R_2 = 1/T_2$. Note that the more rapidly relaxing signal (B) is shorter and broader than (A) yet the total area under the peak is conserved because they are simulated with identical intensities. The differences in linewidths of individual signals can be used to discern site-specific differences in protein dynamics.
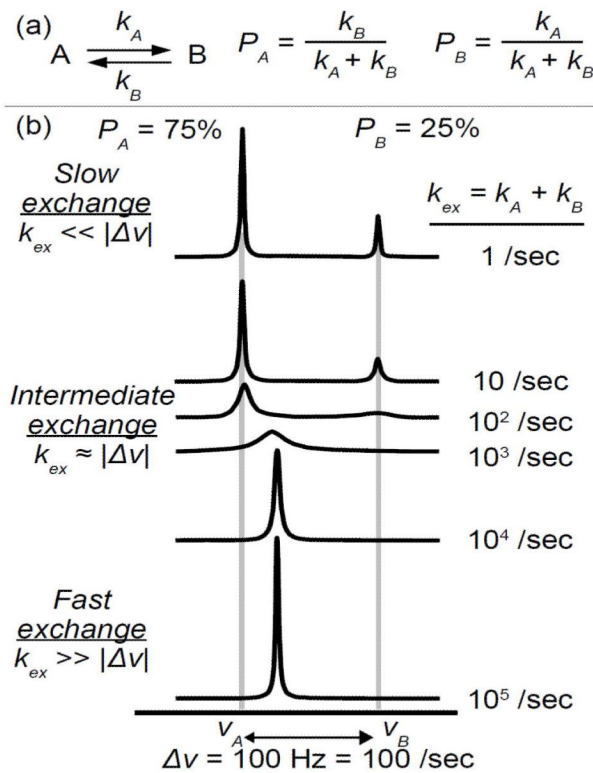
Figure 3.
Chemical exchange processes (including protein dynamics) directly alter the three primary NMR observables. **(a)** Exchange between two states A and B can be described by their rates of departure k_A and k_B and chemical shifts v_A and v_B. k_{ex} is the total exchange rate and P_A and P_B are the population fractions of each state ($P_A + P_B = 1$). **(b)** The effect of varying k_{ex} on NMR spectra with $P_A = 75\%$ and $\Delta v = 100$ Hz. Note that the time regime of chemical exchange is defined by the relative magnitudes of k_{ex} and Δv (each in units of Hz = /sec;see beginning of section 2.2 for details on units). In the slow exchange regime ($k_{ex} \ll |\Delta v|$), signals from both states are observed reflecting their distinct chemical shifts, intensities and linewidths. In the fast exchange regime ($k_{ex} \gg |\Delta v|$), only one signal is observed reflecting the population-weighted averages of chemical shift, intensity and linewidth. In the intermediate exchange regime ($k_{ex} \approx |\Delta v|$), only one signal is observed with intermediate chemical shift. Importantly, the linewidth is increased via "exchange broadening" which can sometimes render this signal undetectable. In each case, the signal linewidths reflect the local dynamics of the sites and the rate of their interconversion. Adapted from [42].
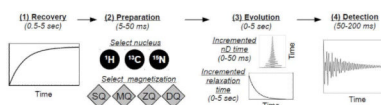
Figure 4.
Four essential steps to any NMR experiment. **(1)** The Recovery period permits restoration of equilibrium magnetization used for detection. **(2)** The Preparation period is used to select the nucleus and quantum magnetization of interest. **(3)** The Evolution period incorporates incremented time delays to permit detection of chemical shift in additional frequency dimensions and/or to permit evolution of relaxation in dynamics experiments. **(4)** The detection period directly observes the FID, which encapsulates the effects of the first three steps. The four steps are typically repeated ~2-32 times to increase the signal to noise ratio via signal averaging. Experiments for measuring dynamics employ a relaxation delay during the evolution period in order to record the decay or buildup of magnetization.
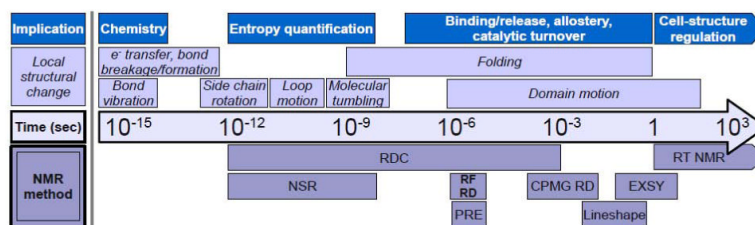
Figure 5.
Protein conformational changes over a broad range of timescales enable their biological function. These dynamic processes can be studied with a variety of NMR methods, eight of which are discussed in this review in the following order: (1) Real Time NMR, RT NMR; (2) EXchange SpectroscopY, EXSY (also known as zz-exchange); (3) Lineshape analysis; (4) Carr-Purcell Meiboom-Gill Relaxation Dispersion, CPMG RD; (5) Rotating Frame Relaxation Dispersion, RF RD; (6) Nuclear Spin Relaxation, NSR; (7) Residual Dipolar Coupling, RDC; (8) Paramagnetic Relaxation Enhancement, PRE.
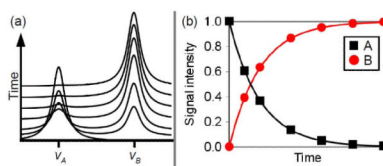
Figure 6.
Real-time NMR reports on interconversion between two species by direct detection of their respective signals. **(a)** After initiating conversion of A→B, a sequence of NMR spectra are recorded in rapid succession with signals from A and B at chemical shifts v_A and v_B respectively. **(b)** The time course of signal intensities can be used to quantify the rate of conversion towards equilibrium.
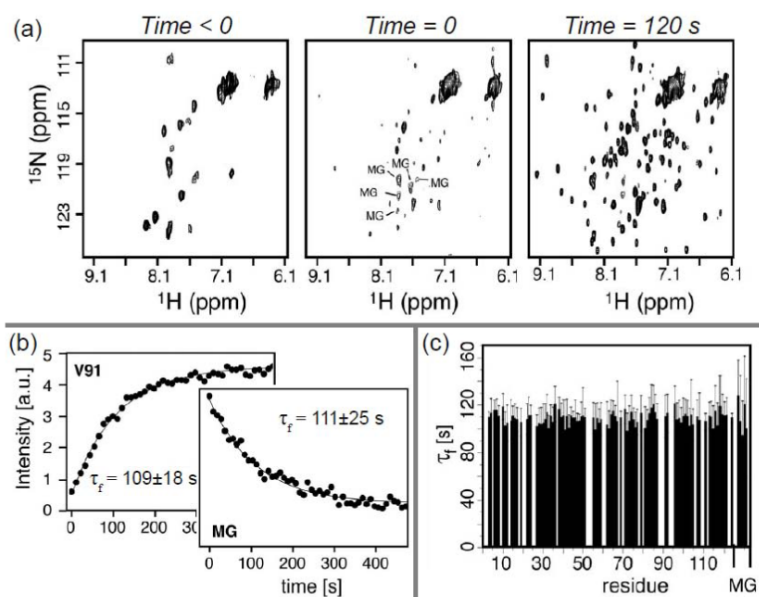
Figure 7.
Folding rate of α-lactalbumin from the molten globule state (MG) monitored by Real-Time NMR. **(a)** 2D NMR spectra acquired before, upon initiation and 120 sec after pH-induced folding reveal site-specific changes in local structure. **(b)** Time-dependence of signal intensity for V91 in the folded state and for an unassigned peak in the MG state fit to a single exponential model. **(c)** The sequence map of individual time constants for the folding process is consistent with global folding at a uniform rate (i.e., no intermediates or local effects). Adapted with permission from [73], copyright 2007 National Academy of Sciences, U.S.A..
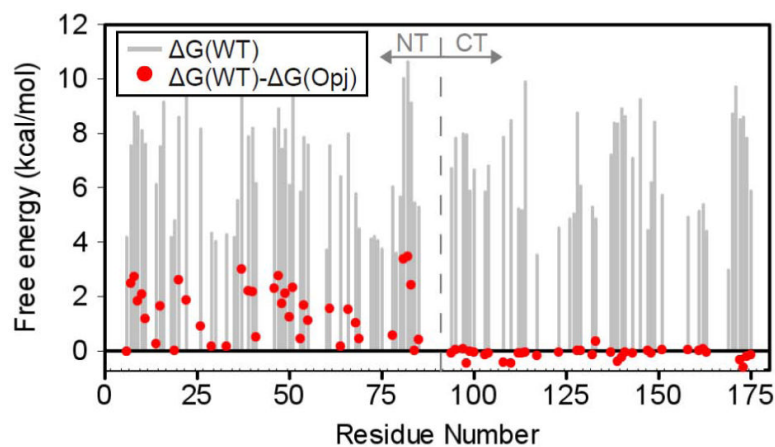
Figure 8.
HDX NMR indicates the Opj mutation of the protein γS crystallin induces selective destabilization of its amino-terminal (NT) domain. Vertical bars indicate ΔG_{op} for the dynamic equilibrium between open and closed states of each amide in the WT protein obtained from fitting site-specific amide proton exchange rates in the EX2 regime. Dots indicate the effect of the mutation on the stability of each residue with positive values indicating destabilization. The Opj mutation reduces the WT ΔG_{Op} by an amount ($\Delta G_{WT} - \Delta G_{Opj}$) = ~1-3 kcal/mol in the NT domain and ~0 kcal/mol in the CT domain. Data courtesy of Zhengrong (Justin) Wu (OSU, personal communication).
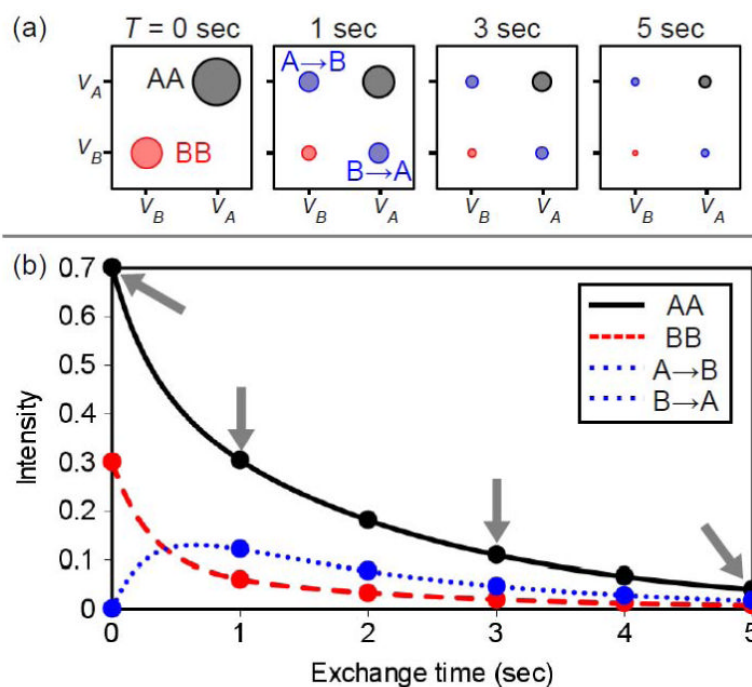
Figure 9.
The EXSY experiment is used to quantify exchange kinetics for structural probes in the slow exchange regime ($k_{ex} << \Delta v$). **(a)** Each structural probe in each molecule is labeled with its chemical shift (v_A or v_B) before and after exchange time T to determine the extent of A↔B interconversion. The resulting NMR spectrum yields up to four signals per exchanging structural probe with intensities modulated in a exchange-time-dependent manner. If a ^1H is exchanging between states A and B with chemical shifts v_A and v_B, exchange crosspeaks will be observed at frequencies (v_A, v_B) and (v_B, v_A). **(b)** The exchange-time-dependent intensities ("build up curves") can be fit to a model of A↔B exchange to define exchange rates k_A and k_B. In the simplified case shown here in which $R_{1A} = R_{1B}$ and $R_{2A} = R_{2B}$ the A→B and B→A signals provide identical information. The intensities of the AA diagonal peaks from the four spectra in (a) are marked with gray arrows.
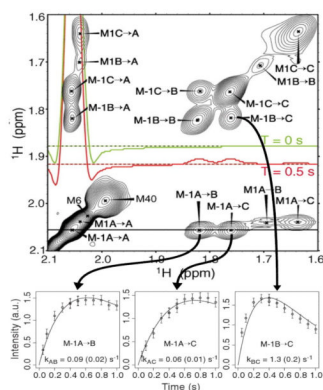
Figure 10.
^1H-^1H 2D EXSY spectrum at $T = 0.5$ sec of the α annulus of the 20S proteasome core particle reveals three-state exchange (A↔B↔C) for methyl probes from two methionione residues ("-1" and "1"). **(Top)** The signals along the diagonal of the spectrum arise from two non-exchanging methionine residues (M6 and M40) and the three exchanging states of M-1 and M1 (A, B and C). Crosspeaks result from exchange between states during the 0.5 sec exchange time. There are 10 such signals resulting from the M-1 and M1 conversions A→B, A→C, B→A, B→C, C→A and C→B (note: M1 B→C and C→B are not observed). The two horizontal cross-sections of the two-dimensional spectrum at $\delta(^1H) = 2.05$ ppm, recorded at $T = 0$ and $T = 0.5$ sec indicate the M-1 A→B and M-1 A→C signals result from exchange as they are absent in the $T = 0$ sec trace. **(Bottom)** The build-up curves are used to determine exchange rate constants and thus inform on the time-dependent structure of the proteasome gate. Adapted from [83].
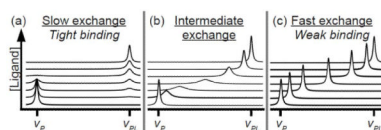
Figure 11.
NMR line shape analysis can be used to study protein-ligand interactions, P + L ↔ PL, by acquiring multiple NMR spectra along a [P] / [L] titration coordinate. The exchange regime

(slow, intermediate or fast) is strongly affected by ligand binding affinity, $K_A = \frac{[PL]}{[P][L]} = \frac{k_{on}}{k_{off}}$ because a tighter-binding complex yields a longer-lived bound state and hence slower exchange between the free and bound states. **(a)** Tight binding yields slow exchange because the protein-ligand complex is long-lived and rarely dissociates during the detection period of the NMR experiment. **(b)** Intermediate exchange results from intermediate binding due to significant interconversion between the free and bound states during the detection period of the NMR experiment. **(c)** Fast exchange results from weak binding because there is extremely rapid interconversion (and hence averaging) during the detection period of the experiment. Adapted from [43].
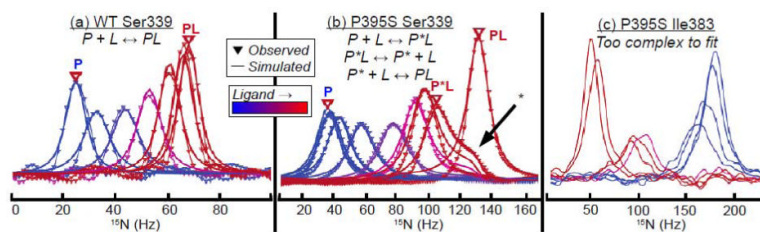
Figure 12.
NMR lineshape analyses reveal transient population of intermediates in SH2 domain-ligand interactions. **(a)** The amide nitrogen of Ser339 in the wild-type (WT) SH2 reports ligand binding in a simple two-state mechanism with signals arising from the free (P) and bound (PL) protein. **(b)** The same probe (Ser339) on SH2 mutant P395S reveals population of an intermediate state (P*L) and a more complex binding mechanism. The arrow marks a shoulder that reflects fast exchange between the P*L and PL states. **(c)** Ile383 on mutant P395S reveals a set of intermediates via titration lineshapes that are too complex to be quantitatively interpreted. Adapted from [104].
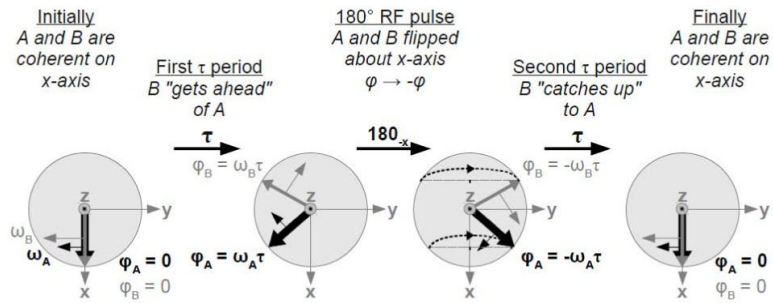
Figure 13.
The spin-echo pulse element τ-$180_{x,y}$-τ serves to refocus magnetization independent of chemical shift. During the first time τ, magnetization of NMR resonances A and B evolve in the x,y-plane under the influence of chemical shifts ω_A and ω_B as evidenced by clockwise rotation about the B_0 field (+z-axis, pointing out of the page). In this example, ω_A and ω_B differ for the two resonances and hence their net phases φ_A and φ_B differ at the end of τ via $\varphi(t) = \omega t$. The 180° pulse along −x flips the magnetization, negating the net phases of A and B. Finally, after evolution for a second period τ, both resonances return to the +x-axis simultaneously ($\varphi(2\tau) = 0$) despite their chemical shift difference: they are "refocused". Importantly, if due to exchange, the average chemical shift $<\omega>$ for a single spin differs in the two τ periods (i.e., if $<\omega_{\tau 1}> \neq <\omega_{\tau 2}>$ via exchange), it will not return to +x at $t = 2\tau$ and hence the set of magnetization vectors will not be refocused completely.
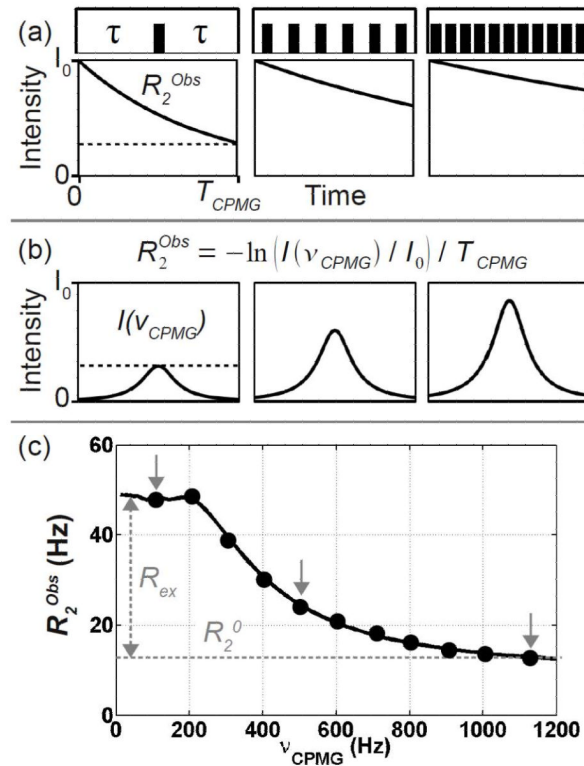
Figure 14.
Carr-Purcell Meiboom-Gill Relaxation Dispersion (CPMG RD) uses spin-echo pulse trains to suppress relaxation due to exchange processes on the μs-ms timescale. **(a)** The number of spin-echo pulses applied during the fixed relaxation time directly determines the CPMG frequency via $\nu_{CPMG} = 1 / (4\tau)$. The applied CPMG pulse train is shown above each relaxation delay (ν_{CPMG} = 100, 500 and 1100 Hz). These pulses reduce the signal relaxation rate during the relaxation delay by refocusing exchange broadening (i.e., reducing R_{ex}). **(b)** The observed signal intensity remaining at the end of the T_{CPMG} relaxation delay is used to obtain an effective relaxation rate $R_2^{Obs}(\nu_{CPMG}) = -\ln(I(\nu_{CPMG})/I_0)/T_{CPMG}$, where I_0 is the signal intensity in the absence of the relaxation delay (i.e., when $T_{CPMG} = 0$). **(c)** The dispersion curve reports on dynamics by plotting relaxation rate as a function of refocusing frequency. R_2^{Obs} is altered in a ν_{CPMG}-frequency-dependent manner such that significant refocusing is typically achieved when ν_{CPMG} exceeds half the exchange rate k_{ex}. The observed relationship between site-specific R_2^{Obs} and ν_{CPMG} is used to fit an exchange model described by the chemical shift differences between the exchanging states $\Delta\nu$, population fraction of the A state P_A with $P_A + P_B = 1$, total exchange rate between the states $k_{ex} = k_A + k_B$, and the intrinsic relaxation rate in the absence of exchange R_2^0, which can be used to determine the exchange broadening R_{ex}. This dispersion curve is simulated using $\Delta\nu = 400$ Hz, $P_A = 90\%$, $k_{ex} = 400$ /sec and $R_2^0 = 10$ Hz with the three ν_{CPMG} values from (a) and (b) marked with vertical arrows. Note that the R_2^{Obs} curve begins to "break" at $\nu_{CPMG} = k_{ex} / 2 = 200$ /sec.
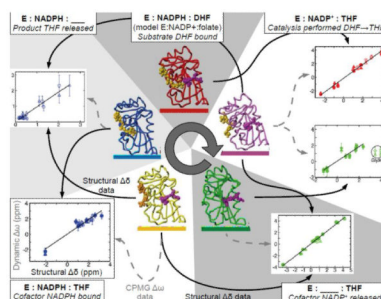
Figure 15.
CPMG RD experiments reveal dynamic "memory" in the catalytic cycle of dihydrofolate reductatse (DHFR). The DHFR catalytic cycle involves five ground-state structures to catalyze conversion of DHF to THF. CPMG RD experiments probing μs-ms flexibility indicate that each ground state samples a structure similar to the adjacent state in the catalytic cycle. This is evidenced by correlation between dynamic $\Delta\omega$ values obtained from fitting CPMG RD data on each state in the cycle and structural $\Delta\delta$ values comparing local conformational differences between states in the cycle. For each correlation, the CPMG $\Delta\omega$ data plotted are connected to the state from which they arise via dashed gray line and structural $\Delta\delta$ data via solid black line. For clarity this is explicitly labeled for the E:NADPH:THF state in the lower left. These observations invite the hypothesis that the motions of DHFR enable its biological function by allowing it to sample the adjacent states at each step in the cycle. Adapted from [120].
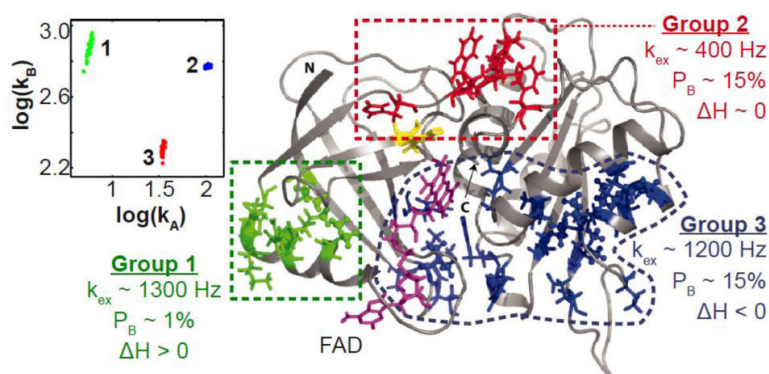
Figure 16.
CPMG RD identifies three groups of independent motions in the structure of FRE-FAD with distinct dynamic motions and biological implications. **(Left)** The (k_A, k_B) plot validates the segregation of site-specific probes into one of three distinct groups. Each point on the plot results from simulations used to estimate fitting errors. Because the three groups of points are well-separated, the uncertainty in fitting the data is much less than the differences in dynamic motions exhibited by the groups. **(Right)** The three groups are mapped to the structure of FRE-FAD. Group 1 appears to undergo a local unfolding process evidenced by enthalpy change $\Delta H > 0$ and magnitude of chemical shift differences $|\Delta \omega_N|$ while groups 2 and 3 directly affect the electron transfer rate in the enzyme due to their proximity to FAD cofactor. Adapted with permission from [115], copyright 2006 National Academy of Sciences, U.S.A.
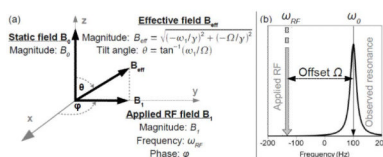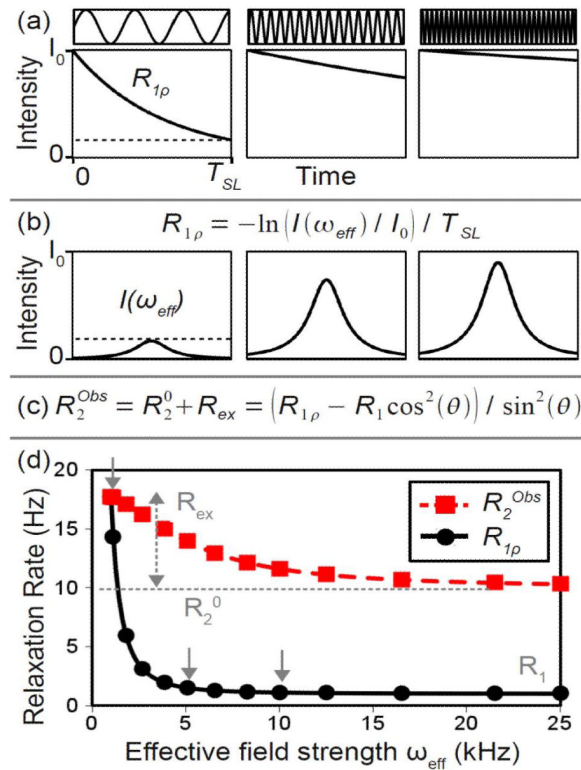
Figure 17.
Effective field B_{eff} arising from the combination of the static magnetic field B_0 and a transient radio frequency (RF) pulse B_1 applied to a spin with a frequency offset Ω from the carrier frequency ω_{RF}. **(a)** An RF pulse has three primary characteristics: (1) carrier frequency ω_{RF}, (2) amplitude B_1 and (3) phase φ. Selective excitation is possible because the combination of B_1 field and static B_0 field produce a frequency-dependent field with a

magnitude $B_{eff} = \sqrt{(-\omega_1/\gamma)^2 + (-\Omega/\gamma)^2}$, and orientation that is tilted an angle $\theta = tan^{-1}(\omega_1/\Omega)$ from the static field B_0. **(b)** The difference in nuclear precession frequency ω_0 and RF carrier frequency ω_{RF} is denoted the resonance offset $\Omega = \omega_0 - \omega_{RF}$. Note that both magnitude and orientation of B_{eff} may differ for each structural probe since they both depend on the site-specific chemical shift ω_0 via resonance offset $\Omega = \omega_0 - \omega_{RF}$.

Figure 18.
Rotating frame relaxation dispersion (RF RD) uses spin-lock pulses to suppress relaxation due to exchange processes on the μs timescale. **(a)** The effective field strength ω_{eff} can be increased by increasing ω_1 while keeping ω_{RF} (and therefore Ω) fixed ("near/on resonance") or by increasing Ω (by changing ω_{RF}) while keeping ω_1 fixed ("off resonance"). The applied spin-lock field is shown above each relaxation delay (ω_{eff} = 1, 5 and 10 kHz). This field reduces the signal relaxation rate during the relaxation delay by refocusing exchange broadening (i.e., reducing R_{ex}). **(b)** The observed signal intensity remaining at the end of the T_{SL} relaxation delay is used to obtain a rotating-frame relaxation rate $R_{1\rho}(\omega_{eff})= -\ln(I(\omega_{eff})/I_0)/T_{SL}$, where I_0 is the signal intensity in the absence of relaxation delay (i.e., when $T_{SL} = 0$). **(c)** The laboratory frame transverse relaxation rate R_2^{Obs} is actually the quantity of interest and can be determined using the known values of offset, $\Omega = \omega_0 - \omega_{RF}$, the rotating frame tilt angle, $\theta = \tan^{-1}(\omega_1/\Omega)$, and a site-specific measure of the longitudinal relaxation rate R_1 by using the relation

$R_2^{Obs}=R_2^0+R_{ex}=\left(R_{1\rho}-R_1\cos^2(\theta)\right)/\sin^2(\theta)$. **(d)** The dispersion curve reports on dynamics by plotting relaxation rate as a function of refocusing frequency. R_2^{Obs} is altered in a frequency-dependent manner such that significant refocusing is typically achieved when ω_{eff} exceeds half the exchange rate k_{ex}. The observed relationship between site-specific R_2^{Obs} and ω_{eff} is used to fit an exchange model. This example illustrates the off-resonance approach whereby ω_1 is fixed at 1 kHz and ω_{eff} is varied via Ω which is varied from 0 to 25 kHz by altering the RF carrier frequency ω_{RF}. The exchange parameters used are $R_1 = 1$ Hz, $R_2^0 = 10$ Hz, $P_A = 80\%$, $k_{ex} = 5,000$ /sec, $\Delta v = 500$ Hz (yields $\Phi_{ex} = 40,000$ Hz^2) with the three ω_{eff} values from (a) and (b) marked with vertical arrows.
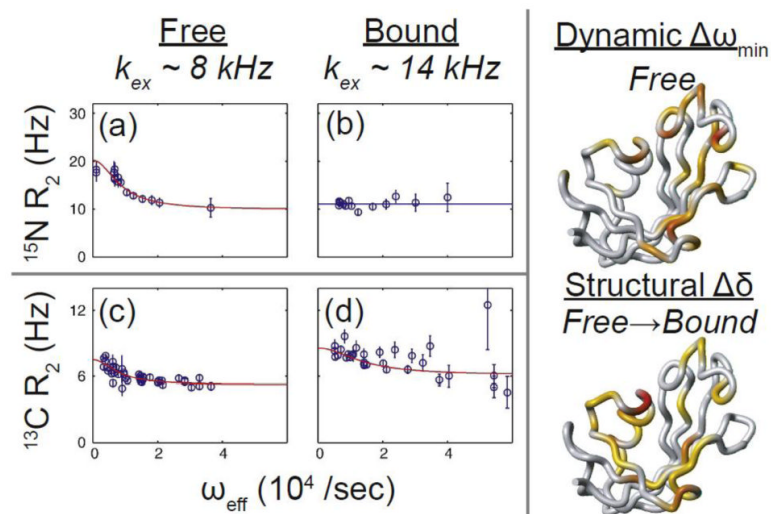
Figure 19.
RF RD reveals differential site-specific changes in backbone ^{15}N and side chain ^{13}C dynamics of the protein FKBP12 upon binding the drug FK506. **(a, b)** The backbone ^{15}N of Ala81 exhibits reduced R_2 relaxation (exchange broadening) upon drug binding (R_{ex} ~10 Hz → 0 Hz). This is consistent with rigidification of the local structure at the µs timescale. **(c, d)** In contrast, the side chain β-^{13}C of the same residue exhibits increased exchange broadening (R_{ex} ~2 Hz → 4 Hz). Importantly, a global fit of all sites in the structure reports an increase in exchange rate k_{ex} from 8,000 to 14,000 /sec upon drug binding. **(Right)** The magnitude of motions in the free protein are mapped onto the structure via the site-specific $\Delta\omega_{min}$ (^{15}N) from RD fits. Similarly, the structural changes induced upon drug-binding are shown via site-specific chemical shift perturbations $\Delta\delta$(^{15}N) from NMR spectra. This is consistent with a model in which drug binding alters the structure of FKBP12, rigidifying the backbone while increasing flexibility of the side chains. Adapted from [156].
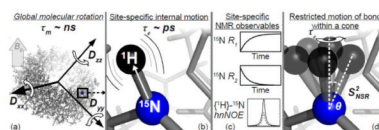
Figure 20.
Molecular motion at the ps-ns timescale is indirectly detected via nuclear spin relaxation (NSR). NSR is stimulated by MHz-frequency oscillating magnetic fields arising from (i) dipole-dipole (DD) interactions, (ii) chemical shift anisotropy (CSA) and (iii) quadrupolar interactions due to reorientation of bonds from **(a)** molecular rotation (tumbling on the ns timescale) with respect to the static B_0 field, and **(b)** site-specific internal motions on the ps timescale. **(c)** The site-specific NMR observables related to NSR include the longitudinal recovery rate R_1, the transverse relaxation rate R_2 and the heteronuclear *NOE*. **(d)** These observables can constrain a model of global and internal motion at the ps-ns timescale. This is often interpreted via the modelfree or reduced spectral density mapping approach, either of which can be used to describe restricted motion of each bond vector within a cone of angle θ (larger $S^2 \rightarrow$ smaller θ) with intra-cone diffusion rate via τ_e and the molecular rotational diffusion time τ_m via diffusion tensor elements (D_{xx}, D_{yy}, D_{zz}) shown in (a).
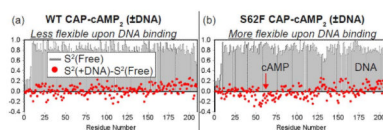
Figure 21.
NSR and modelfree analyses indicate that DNA binding decreases ps-ns flexibility for effector-bound WT CAP, but increases flexibility for effector-bound S62F CAP. Calorimetry experiments corroborate this finding at a global level by indicating that DNA binding is driven by enthalpy ΔH for WT CAP but by entropy ΔS for S62F CAP. **(a,b)** Site-specific rigidity and its change upon DNA-binding are mapped to the sequence via the order parameter $S^2(Free)$ as vertical bars and the change in S^2, $\Delta S^2 = S^2(+DNA) - S^2(Free)$, as dots for WT (a) and S62F (b). Negative values of ΔS^2 indicate regions of the S62F protein that become more flexible upon binding DNA, especially in the cAMP binding site (red arrow). This provides high-resolution mechanistic details of the dynamic linkage between the cAMP site and the DNA site. The cAMP site includes about half the residues between 60-85 and the DNA site includes about half the residues between 165-200 (within 5Å of crystal structure PDB ID 1CGP) [118]. Data courtesy of Charalampos (Babis) Kalodimos (Rutgers Univ., personal communication).
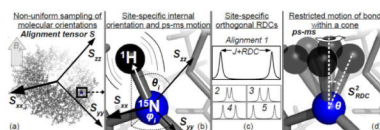
Figure 22.
Molecular motion at the ps-ms timescale is indirectly detected via residual dipolar couplings (RDCs). **(a,b)** RDCs are affected by (i) non-uniform sampling of molecular orientations (i.e., anisotropic rotation) with respect to the magnetic field B_0, (ii) site-specific orientations of each bond vector with respect to the molecule and (iii) site-specific ps-ms motions of each bond vector with respect to the molecule. **(c)** To extract the dynamic information, the site-specific RDCs are measured using a non-decoupled NMR spectrum which splits each signal by an amount $J+RDC$. Each of at least five orthogonal alignment media yield unique alignment tensors and potentially unique values of the RDC splitting. All RDC data are analyzed together by (1) fitting a unique alignment tensor $S = (S_{xx}, S_{yy}, S_{zz})$ shown in (a) for each alignment medium, (2) fitting a site-specific ps-ms order parameter S^2_{RDC} for all alignment media and (3) obtaining site-specific bond vector orientations (θ_i, φ_i) with respect to the molecular frame shown in (b) used for all alignment media. The (θ_i, φ_i) values are obtained from a high-resolution structural model. **(d)** This can be used to describe restricted motion of each bond vector within a cone of angle θ (larger $S^2_{RDC} \rightarrow$ smaller θ) sampled within the ps-ms time window.
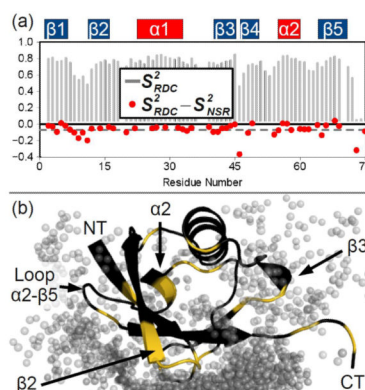
Figure 23.
RDCs reveal ps-ms dynamics of ubiquitin apparently related to the conformational selection during target binding. **(a)** Site-specific order parameters from the RDC EROS ensemble S^2_{RDC} probe ps-ms rigidity. Subtraction of order parameters from nuclear spin relaxation S^2_{NSR} (ps-ns) reveals negative values reflecting flexibility in the previously unprobed "supra-τ_c" (ns-ms) time window. The average value of $S^2_{RDC} - S^2_{NXR}$ (−0.07) is marked with a horizontal dashed gray line. **(b)** $S^2_{RDC} - S^2_{NSR}$ values less than the average are colored gold on the structure of ubiquitin to indicate ns-ms flexibility. This flexibility is mostly limited to the loops whereas the α helices and β strands are rigid in this time window. Some regions including the NT end of β2 are coincident with the gray spheres representing contacting atoms from target proteins in complex with ubiquitin observed via crystallography. Consequently, the ns-ms flexibility at these key locations may enhance the conformational selection mechanism of ubiquitin for its many binding partners. Overall, inclusion of RDC data improve temporal coverage in studies of protein motions and are important to help address the linkage of structure, dynamics and function [184,202]. Data courtesy of Oliver Lange, Bert de Groot and Christian Griesinger (Max Planck Inst., personal communication).
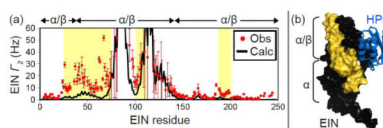
Figure 24.
Intermolecular PREs indicate non-nonspecific encounters between the proteins EIN and HPr. **(a)** Site-specific ^1HN Γ_2 rates of EIN result from both specific and non-specific contacts with PRE-labeled HPr and are shown as red dots. The contributions from specific contacts are calculated using a high-resolution structural model of the stereospecific EIN-HPr complex and are shown as a black line. Observed values of Γ_2 that exceed the calculated values result from one or more transiently populated non-specific binding modes. **(b)** The points of non-specific contact between EIN and HPr are shown in gold. Based on the Γ_2 data in (a), these residues are 25-75, 100-110 and 190-200. These data reveal the nature of non-specific encounter complexes between EIN and HPr that describe how the proteins encounter one another in solution [191]. Data courtesy of Chun Tang (U. Missouri, personal communication).

Table 1

Three possible dynamic relationships between a pair of structural probes

Dynamic relationship	(k_A, k_B)	$\left(\dfrac{\Delta k_{A,B}}{\Delta Condition}\right)$	Macroscopic protein example	Macroscopic analogy
Same process	Same	Quantitatively the same	Hinged motion of entire domain *(both probes near hinge)*	Two children on different sides of the same see-saw
Independent processes	Same or different	Same or different	Floppiness of distant loops *(each probe in different loop)*	Two children on different swings
Coupled processes	Same or different	Qualitatively the same	Contacting loops / domains *(each probe in different loop / domain)*	One child pushing another on a swing